Original Paper

Improved probabilistic seismic AVO inversion constrained by instantaneous phase using quadratic PP-reflectivity approximation and IA2RMS-Gibbs algorithm

Shuang-Shuang Zhou [a,b,c], Xing-Yao Yin [a,b,c,*], Kun Li [a,c,d], Ya-Ming Yang [a,b,c]

[a] State Key Laboratory of Deep Oil and Gas, China University of Petroleum (East China), Qingdao, 266580, Shandong, China
[b] School of Geosciences, China University of Petroleum (East China), Qingdao, 266580, Shandong, China
[c] Laoshan Laboratory, Qingdao, 266580, Shandong, China
[d] College of Computer Science and Technology, China University of Petroleum (East China), Qingdao, 266580, Shandong, China

ARTICLE INFO

ABSTRACT

Seismic amplitude variation with offset (AVO) inversion is a cornerstone of oil and gas reservoir prediction, enabling the estimation of subsurface elastic parameters and characterization of stratigraphic interfaces. However, balancing inversion accuracy and computational efficiency remains a critical challenge. To address this, we propose a novel probabilistic AVO inversion framework integrating three key innovations. First, we derive a high-precision quadratic approximation for compressional (P-wave) reflectivity by retaining first- and second-order terms from the exact Zoeppritz equations through a perturbation strategy. This approach significantly enhances accuracy compared to conventional linear approximations, particularly in reflecting the true amplitude variation at large angles. Subsequently, to improve lateral continuity and stratigraphic resolution, we introduce an instantaneous phase constraint derived via the Hilbert transform. This constraint leverages phase sensitivity to seismic waveform coherence, ensuring geologically consistent interface characterization during stochastic inversion. Furthermore, we develop a hybrid Markov Chain Monte Carlo (MCMC) algorithm combining adaptive Gibbs sampling with the independent doubly adaptive rejection Metropolis sampling (IA2RMS) method. This framework efficiently samples high-dimensional posterior probability density functions (PDFs) of elastic parameters: Gibbs sampling generates adaptive proposal distributions, while IA2RMS accelerates Markov chain convergence through location- and scale-adjustable proposals. Numerical experiments and field seismic data demonstrate the robustness and feasibility of the proposed probabilistic AVO inversion method.

1. Introduction

Seismic amplitude variation with offset (AVO) inversion method plays an extremely important role in oil and gas reservoir prediction, which is an effective way to obtain various elastic parameters of the subsurface medium and reveal the distribution, physical properties and hydrocarbon properties of the subsurface reservoir (Yin et al., 2015; Li et al., 2020; Pan et al., 2021; Dai et al., 2022; Yu et al., 2023). As oil and gas reservoirs continue

to be developed and exploited, the accuracy of geophysical inversion methods for deep or complex geological formations is becoming more demanding (Chen et al., 2020a,b; Li et al., 2021; Li et al., 2022a; Chen and Innanen, 2023). Compared to conventional deterministic inversion methods (Li and Zhang, 2017; Ajaz et al., 2021; Yang et al., 2022), stochastic inversion methods (Pan et al., 2017) have certain advantages in identifying oil and gas reservoirs with thin inter-tuning effects, so stochastic inversion techniques with higher reservoir prediction accuracy have come

---

into being. The Monte Carlo method (also known as the statistical simulation method) is one of the more common methods of optimization search (Geman and Geman, 1984), in which the samples are randomly drawn from a sample space, and the mean and variance of the samples are finally used to estimate the statistical characteristics of the overall model parameters. The Metropolis algorithm (Metropolis et al., 1953) was first proposed by Metropolis, based on which Hasting developed the Metropolis-Hastings (MH) algorithm. The Markov Chain Monte Carlo (MCMC) stochastic inversion method is a widely used heuristic nonlinear stochastic inversion approach within Monte Carlo methods. The advantage of the heuristic algorithm (Fjeldstad and Omre, 2020) over the non-heuristic algorithm (Zhi et al., 2016; Cheng et al., 2019; Zhou et al., 2022) is that the problem of integral operations and local polarization, which are difficult to solve in Bayesian algorithms, are avoided, so that the global optimal solution of the inverse problem is better solved (Conti et al., 2013). In geophysical inversion problems, we typically use Markov Chain Monte Carlo algorithms to evaluate the uncertainty in the a priori models and posterior probabilities of the parameters (Chen et al., 2017). The solution of a probabilistic inverse problem is usually expressed in terms of a posteriori probability density functions, which can also be represented by multiple realizations of the model (Ely et al., 2018). Since the petrophysical model (Grana, 2022) is a bridge between elastic parameters such as velocity, density, impedance and other relevant reservoir physical properties such as lithology and porosity (Figueiredo et al., 2018), this relationship can be used as a constraint on the spatial correlation of stochastic simulations (Huang et al., 2021). Different physical characteristics and elasticity parameters in the same region usually present different Gaussian or non-Gaussian distributions (Fjeldstad and Grana, 2018), and the distributions mixed together by these attributes are called mixed Gaussian distributions (Guo et al., 2021), which can be sampled by the MCMC method to obtain the multimodal posterior distributions of the model parameters (Figueiredo et al., 2019). The MCMC method can effectively improve the vertical resolution of reservoir prediction, however, how to solve the computational efficiency and lateral resolution of the method (Robert et al., 2018) has been a difficult problem. Martino et al. (2015) and Li et al. (2022b) introduced an adaptive MCMC algorithm (Zhang and Taflanidis, 2019) that effectively accelerates the convergence of Markov chains and improves inversion efficiency. Meanwhile, the implementation of higher-order approximation (Zhang et al., 2015; Yang et al., 2023) in pre-stack seismic inversion establishes a robust framework that achieves optimal balance between computational stability, processing efficiency, and inversion fidelity. This methodology substantially overcomes limitations inherent in conventional weak-contrast assumptions for neighboring geological units, exhibiting superior performance in scenarios with increased impedance contrasts. There are many factors affecting the accuracy of geophysical inversion, such as the multiple solutions of seismic inversion as well as the noise effect of seismic data and the limited resolution, but MCMC is an inversion method by evaluating the uncertainty of elastic or physical parameters, which determines that the method is more noise-resistant compared to deterministic inversion. In the identification of oil and gas reservoirs with thin mutual tuning effect, the accuracy and stability of the inversion are greatly affected by the noise. Pei et al. (2022) took advantage of the property that the instantaneous phase of seismic traces is

sensitive to the weak changes of seismic signals, and use the instantaneous phase as the constraint of the objective function for the inversion, by which the seismic thin layers can be effectively identified, and the accuracy of the inversion and the speed of convergence can be improved. Therefore, it is crucial to carry out probabilistic AVO inversion that can simultaneously improve the stability, convergence speed, acceptance rate, lateral continuity, and inversion accuracy of stochastic inversion.

In this study, we first derive novel higher-order approximation equations to enhance the accuracy and stability of stochastic inversion. Given the seismic response's heightened sensitivity to elastic parameters' higher-order terms, we implement a perturbation strategy that retains both first- and second-order terms in the elastic parameter expansions. Subsequently, we develop an enhanced IA2RMS-Gibbs sampler incorporating adaptive proposal distributions that progressively converge to the posterior probability distribution, thereby enabling efficient high-dimensional Bayesian inference. Furthermore, we propose a probabilistic seismic AVO inversion framework constrained by instantaneous phase information. The instantaneous phase constraints are integrated into the Bayesian framework through Hilbert transform-derived relationships, significantly improving sensitivity to low-reflectivity zones in seismic data and enhancing thin-bed reservoir identification capability. The model experiment and a field data application are utilized to demonstrate the feasibility and stability of the proposed method.

2. Theory and method

2.1. Derivation of second order approximation for PP-reflectivity

The formulas for the reflection and transmission coefficients in the case of plane wave incidence were derived by the famous German physicist Zoeppritz (1919) on the basis of the fluctuation equation and the theory of elasticity. The reflection and transmission can be expressed as follows:

$$\underbrace{\begin{bmatrix} -\sin\alpha_1 & -\cos\beta_1 & \sin\alpha_2 & \cos\beta_2 \\ \cos\alpha_1 & -\sin\beta_1 & \cos\alpha_2 & -\sin\beta_2 \\ \sin 2\alpha_1 & \mathbf{A}_{32} & \mathbf{A}_{33} & \mathbf{A}_{34} \\ \cos 2\beta_1 & \mathbf{A}_{42} & \mathbf{A}_{43} & \mathbf{A}_{44} \end{bmatrix}}_{\mathbf{A}} \underbrace{\begin{bmatrix} R_{PP} \\ R_{PS} \\ T_{PP} \\ T_{PS} \end{bmatrix}}_{\mathbf{B}} = \underbrace{\begin{bmatrix} \sin\alpha_1 \\ \cos\alpha_1 \\ \sin 2\alpha_1 \\ -\cos 2\beta_1 \end{bmatrix}}_{\mathbf{C}}$$

(1)

with

$$\mathbf{A}_{32} = \frac{V_{P1}}{V_{S1}}\cos 2\beta_1, \quad \mathbf{A}_{33} = \frac{V_{P1}}{V_{P2}}\frac{V_{S2}^2}{V_{S1}^2}\frac{\rho_2}{\rho_1}\sin 2\alpha_2,$$

$$\mathbf{A}_{34} = -\frac{V_{P1}V_{S2}}{V_{S1}^2}\frac{\rho_2}{\rho_1}\cos 2\beta_2, \quad \mathbf{A}_{42} = -\frac{V_{S1}}{V_{P1}}\sin 2\beta_1,$$

$$\mathbf{A}_{43} = -\frac{\rho_2}{\rho_1}\frac{V_{P2}}{V_{P1}}\cos 2\beta_2, \quad \mathbf{A}_{44} = -\frac{\rho_2}{\rho_1}\frac{V_{S2}}{V_{P1}}\sin 2\beta_2,$$

where V_P, V_S and ρ are denoted as longitudinal (P-) wave, transverse (S-) wave velocities and the bulk density, respectively; α and β represent the angles of incidence of P- and S-waves, respectively. The subscripts 1 and 2 indicate the parameters of the layers above and below the reflection interface, respectively.

To assess the reflection coefficients dependent on the angle of incidence, we obtain the second-order partial derivatives from Eq. (1) in terms of the three parameters:

$$p_1 = \frac{\Delta V_P}{\overline{V}_P}, \ p_2 = \frac{\Delta V_S}{\overline{V}_S}, \ p_3 = \frac{\Delta \rho}{\overline{\rho}}, \tag{2}$$

where ΔV_P and $\overline{V}_P$ are the difference and average value of P-wave velocity of the upper and lower layers of the interface, and correspondingly for ΔV_S, $\overline{V}_S$, $\Delta \rho$, and $\overline{\rho}$. The second-order partial derivative operator can be expressed as follows:

$$\Delta_2 = p_i p_j \frac{\partial}{\partial p_i \partial p_j} \bigg|_{p_i=0,p_j=0} \tag{3}$$

It is worth noting that we should take into the consideration the special case where the plane waves incident on the upper and lower layers of the interface are the same, that is, $p_i = 0$ ($i = 1, 2, 3$). Then, Eq. (1) can be expressed as

$$\mathbf{A}_0 \mathbf{B}_0 = \mathbf{C}_0 \tag{4}$$

where $\mathbf{A}_0 = \mathbf{A}|_{p_i=0}$, $\mathbf{B}_0 = \mathbf{B}|_{p_i=0}$, and $\mathbf{C}_0 = \mathbf{C}|_{p_i=0}$ are the undisturbed terms. Considering the first- and second-order perturbations for all small quantities p_i ($i = 1, 2, 3$), the matrix $\mathbf{A}$ and vectors $\mathbf{B}$ and $\mathbf{C}$ can be written as follows:

$$\mathbf{A} = \mathbf{A}_0 + \mathbf{A}' + \mathbf{A}'' + \cdots, \ \mathbf{B} = \mathbf{B}_0 + \mathbf{B}' + \mathbf{B}'' + \cdots, \ \mathbf{C}$$
$$= \mathbf{C}_0 + \mathbf{C}' + \mathbf{C}'' + \cdots. \tag{5}$$

The second-order matrix representation of Eq. (1) can be written as

$$(\mathbf{A}_0 + \mathbf{A}' + \mathbf{A}'')(\mathbf{B}_0 + \mathbf{B}' + \mathbf{B}'') = (\mathbf{C}_0 + \mathbf{C}' + \mathbf{C}'') \tag{6}$$

According to Eq. (6), the first order approximation equation can be expressed as: $\mathbf{A}' \mathbf{B}_0 + \mathbf{A}_0 \mathbf{B}' = \mathbf{C}'$. For the second-order terms of Eq. (6), expanding it yields the following equation:

$$\mathbf{A}'' \mathbf{B}_0 + \mathbf{A}' \mathbf{B}' + \mathbf{A}_0 \mathbf{B}'' = \mathbf{C}''. \tag{7}$$

The analytic form of the second order matrix for reflection and transmission (Yang et al., 2023) can be expressed as follows:

$$\mathbf{B}'' = \mathbf{A}_0^{-1} (\mathbf{C}'' - \mathbf{A}'' \mathbf{B}_0 - \mathbf{A}' \mathbf{B}'), \tag{8}$$

with

$$\mathbf{A}'' = \begin{bmatrix} A''_{11} & A''_{12} & A''_{13} & A''_{14} \\ A''_{21} & A''_{22} & A''_{23} & A''_{24} \\ A''_{31} & A''_{32} & A''_{33} & A''_{34} \\ A''_{41} & A''_{42} & A''_{43} & A''_{44} \end{bmatrix}, \ \mathbf{C}'' = \begin{bmatrix} C''_{11} \\ C''_{21} \\ C''_{31} \\ C''_{41} \end{bmatrix},$$

$$A''_{11} = \frac{\Delta V_P^2 \cos \alpha \tan \alpha}{8 \overline{V}_P^2}, \ A''_{12} = \frac{\Delta V_S^2 \sin \beta \tan \beta}{8 \overline{V}_S^2},$$

$$A''_{13} = C''_{11} = \frac{\Delta V_P^2 \cos \alpha \tan \alpha}{8 \overline{V}_P^2}, \ A''_{14} = -\frac{\Delta V_S^2 \sin \beta \tan \beta}{8 \overline{V}_S^2},$$

$$A''_{21} = A''_{23} = C''_{21} = -\frac{\Delta V_P^2 \sin \alpha \tan \alpha}{8 \overline{V}_P^2}, \ A''_{22} = A''_{24}$$

$$= \frac{\Delta V_S^2 \cos \beta \tan \beta}{8 \overline{V}_S^2}, \ A''_{31} = C''_{31} = \frac{\Delta V_P^2 \sin 2\alpha \tan^2 \alpha}{8 \overline{V}_P^2},$$

$$A''_{32} = \frac{\Delta V_P \Delta V_S (2 \sin 2\beta \tan \beta - \cos 2\beta)}{4 \overline{V}_S^2}$$
$$- \frac{\Delta V_S^2 \overline{V}_P (2 \sin 2\beta \tan \beta - \cos 2\beta + 2 \cos 2\beta \tan^2 \beta)}{4 \overline{V}_S^3},$$

$$A''_{33} = \frac{\Delta \rho^2 \sin 2\alpha}{2 \overline{\rho}^2} + \frac{2 \Delta V_S^2 \sin 2\alpha}{\overline{V}_S^2} + \frac{2 \Delta \rho \Delta V_S \sin 2\alpha}{\overline{\rho} \overline{V}_S}$$
$$- \frac{\Delta \rho \Delta V_P (\sin 2\alpha - \cos 2\alpha \tan \alpha)}{\overline{\rho} \overline{V}_P}$$
$$- \frac{2 \Delta V_P \Delta V_S (\sin 2\alpha - \cos 2\alpha \tan \alpha)}{\overline{V}_P \overline{V}_S}$$
$$+ \frac{\Delta V_P^2 (\sin 2\alpha - 2 \cos 2\alpha \tan \alpha - \sin 2\alpha \tan^2 \alpha)}{2 \overline{V}_P^2},$$

$$A''_{34} = -\frac{\Delta V_S^2 \overline{V}_P (-5 \cos 2\beta + 6 \sin 2\beta \tan \beta + 2 \cos 2\beta \tan^2 \beta) \cos 2\beta}{4 \overline{V}_S^3}$$
$$- \Delta V_S \Delta V_P \left(\frac{2 \cos 2\beta - \sin 2\beta \tan \beta}{4 \overline{V}_S^2} + \frac{\Delta \rho \Delta V_P \cos 2\beta}{2 \Delta V_S} \right)$$
$$- \frac{\Delta \rho \Delta V_S \overline{V}_P (3 \cos 2\beta - 2 \sin 2\beta \tan \beta)}{2 \overline{\rho} \overline{V}_S^2} - \frac{\Delta \rho^2 \overline{V}_P \cos 2\beta}{2 \overline{\rho}^2 \overline{V}_S},$$

$$A''_{41} = -C''_{41} = \frac{\Delta V_S^2 \cos 2\beta \tan^2 \beta}{2 \overline{V}_S^2},$$

$$A''_{42} = \frac{\Delta V_P^2 \overline{V}_S \sin 2\beta}{4 \overline{V}_P^3} + \frac{\Delta V_P \Delta V_S (\sin 2\beta + 2 \cos 2\beta \tan \beta)}{4 \overline{V}_P^2}$$
$$+ \frac{\Delta V_S^2 (-\cos 2\beta \tan \beta + \sin 2\beta \tan^2 \beta)}{2 \overline{V}_P \overline{V}_S},$$

$$A''_{43} = -\frac{\Delta \rho^2 \cos 2\beta}{2 \overline{\rho}^2} - \frac{\Delta \rho \Delta V_P (\cos 2\beta - \sin 2\beta \tan \beta)}{\Delta V_P}$$
$$+ \frac{\Delta V_P^2 (-\cos 2\beta + 2 \sin 2\beta \tan \beta + \cos 2\beta \tan^2 \beta)}{2 \overline{V}_P^2},$$

$$A''_{44} = \frac{\Delta V_P \Delta V_S (-\sin 2\beta - 2 \cos 2\beta \tan \beta)}{4 \overline{V}_P^2} - \frac{\Delta V_P^2 \overline{V}_S \sin 2\beta}{4 \overline{V}_P^3}$$
$$- \frac{\Delta \rho \Delta V_S (\sin 2\beta + 2 \cos 2\beta \tan \beta)}{2 \overline{\rho} \overline{V}_P} - \frac{\Delta \rho \Delta V_P \overline{V}_S \sin 2\beta}{2 \overline{\rho}}$$
$$+ \frac{\Delta V_S^2 (-\cos 2\beta \tan \beta + \sin 2\beta \tan^2 \beta)}{2 \overline{V}_P \overline{V}_S} - \frac{\Delta \rho^2 \overline{V}_S \sin 2\beta}{2 \overline{\rho}^2 \overline{V}_P},$$

where $\mathbf{A}'$ and $\mathbf{B}'$ are conventional first-order approximation matrix, and it is worth mentioning that we derive novel second-order approximation matrix ($\mathbf{A}''$ and $\mathbf{C}''$) based on Snell's rule and the Aki approximation (Aki and Richards, 1980). $\mathbf{B}_0 = [0, 0, 1, 0]^T$ is a vector that is not all zero. The inverse of the matrix $\mathbf{A}_0$ can be derived using the Cramer's rule as follows:

$$
\mathbf{A}_0^{-1} = \begin{bmatrix}
-\dfrac{\overline{V}_S^2}{\overline{V}_P^2}\sin\alpha & \dfrac{1 - 2\dfrac{\overline{V}_S^2}{\overline{V}_P^2}\sin^2\alpha}{2\cos\alpha} & \dfrac{\sin\alpha}{2\overline{\rho}\,\overline{V}_P\cos\alpha} & -\dfrac{1}{2\overline{\rho}\,\overline{V}_P} \\[3ex]
-\dfrac{1 - 2\dfrac{\overline{V}_S^2}{\overline{V}_P^2}\sin^2\alpha}{2\cos\beta} & -\dfrac{\overline{V}_S}{\overline{V}_P}\sin\alpha & \dfrac{1}{2\overline{\rho}\,\overline{V}_S} & \dfrac{\sin\alpha}{2\overline{\rho}\,\overline{V}_P\cos\beta} \\[3ex]
\dfrac{\overline{V}_S^2}{\overline{V}_P^2}\sin\alpha & \dfrac{1 - 2\dfrac{\overline{V}_S^2}{\overline{V}_P^2}\sin^2\alpha}{2\cos\alpha} & \dfrac{\sin\alpha}{2\overline{\rho}\,\overline{V}_P\cos\alpha} & \dfrac{1}{2\overline{\rho}\,\overline{V}_P} \\[3ex]
\dfrac{1 - 2\dfrac{\overline{V}_S^2}{\overline{V}_P^2}\sin^2\alpha}{2\cos\beta} & -\dfrac{\overline{V}_S}{\overline{V}_P}\sin\alpha & \dfrac{1}{2\overline{\rho}\,\overline{V}_S} & -\dfrac{\sin\alpha}{2\overline{\rho}\,\overline{V}_P\cos\beta}
\end{bmatrix}
\tag{9}
$$

The second order approximation of PP reflectivity consists of a combination of two parts—a first order term and a second order term, expressed analytically as follows:

$$R_{PP}(\alpha) = R_1(\alpha) + R_2(\alpha), \tag{10}$$

where

$$R_1(\alpha) = \frac{1}{2}\frac{\Delta V_P}{\overline{V}_P}\left(1 + \sin^2\alpha + \sin^2\alpha\tan^2\alpha\right) + \frac{1}{2}\frac{\Delta\rho}{\overline{\rho}}\left(1 - 4h^2\sin^2\alpha\right)$$
$$-4h^2\frac{\Delta V_S}{\overline{V}_S}\sin^2\alpha,$$

$$R_2(\alpha) = \frac{h^3\sin\alpha\tan\alpha}{2\sqrt{1 - h^2\sin^2\alpha}}\left(1 - 2h^2\sin^2\alpha + \cos^2\alpha\right)\left(\frac{\Delta\rho}{\overline{\rho}} + \frac{2\Delta V_S}{\overline{V}_S}\right)^2$$
$$-\frac{h\sin\alpha\tan\alpha}{\sqrt{1 - h^2\sin^2\alpha}}\left(\frac{1}{4} - \frac{1}{2}h^2\sin^2\alpha\right)\left(\frac{\Delta\rho}{\overline{\rho}}\right)^2$$
$$-\frac{2h^3\sin^3\alpha\tan\alpha}{\sqrt{1 - h^2\sin^2\alpha}}\left(\frac{\Delta V_S}{\overline{V}_S}\right)^2,$$

where $h = \overline{V}_S/\overline{V}_P$ is the ratio of the averages of the S- and P-wave velocities. The construction of the forward operator based on the approximate second order analytical formulation of Eq. (10) is shown in Appendix A.

2.2. Instantaneous phase constraints

Within the geophysical domain, instantaneous phase (Abreu et al., 2019; Pei et al., 2022) is exceptionally sensitive to seismic response, and interface information and discontinuities in the stratigraphy can be effectively reflected. Therefore, in this section, we propose to add the constraints of instantaneous phase in the seismic inversion so as to effectively improve the lateral continuity and vertical resolution of the seismic inversion method.

Typically, the seismic data we apply is the real part of the complex signal, and the imaginary part of the seismic signal is represented by the Hilbert transform (HT) of the seismic data, then the complex domain of the seismic signal can be expressed as:

$$\tilde{\mathbf{d}} = \mathbf{d} + i\widehat{\mathbf{d}} \tag{11}$$

where $\tilde{\mathbf{d}}$ represents the complex signal of the seismic signal, $\mathbf{d}$ represents the seismic data, and $\widehat{\mathbf{d}} = \text{Hilbert}(\mathbf{d})$ represents Hilbert transform of the seismic data.

The instantaneous phase of the seismic data can be calculated using the Hilbert transform, which is expressed as:

$$\mathbf{P} = \tan^{-1}\left(\widehat{\mathbf{d}} \big/ \mathbf{d}\right) \tag{12}$$
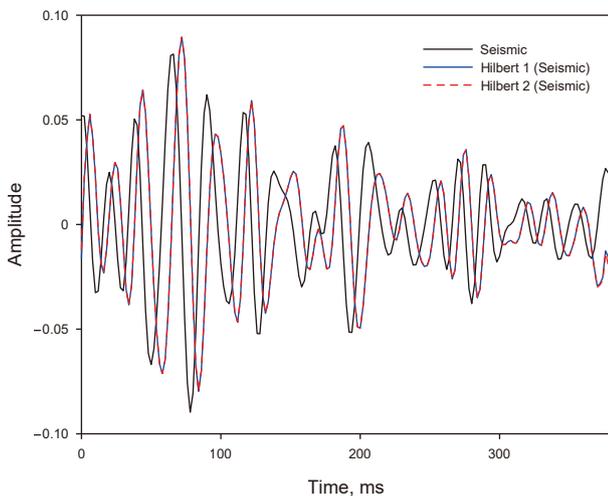
with

Fig. 1. Comparison of Hilbert transforms of seismic signals. The black curve represents the noise-free synthetic seismic data, the blue curve represents the Hilbert transform curve calculated by the equation $\widehat{\mathbf{d}} = \text{Hilbert}(\mathbf{G}_1\mathbf{m} + \mathbf{G}_2[(\mathbf{Qm})\circ(\mathbf{Qm})])$, and the red dotted curve represents the Hilbert transform curve calculated by the equation $\widehat{\mathbf{d}} = \mathbf{G}_{H1}\mathbf{m} + \mathbf{G}_{H2}[(\mathbf{Qm})\circ(\mathbf{Qm})]$.
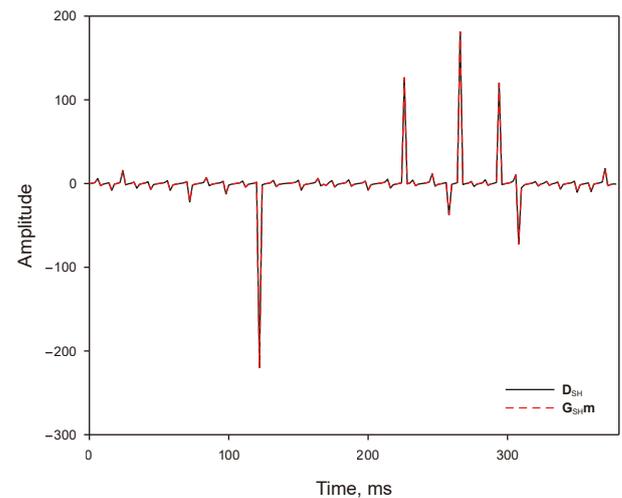

Fig. 2. Comparison of instantaneous phase constraint terms for seismic signals. The black curve is calculated from equation $\mathbf{D}_{SH} = \tan(\mathbf{P})$, and the red dotted curve is calculated from equation $\mathbf{G}_{SH}\mathbf{m} = \mathbf{G}_{SH1}\mathbf{m} + \mathbf{G}_{SH2}[(\mathbf{Qm})\circ(\mathbf{Qm})]$.

$$\mathbf{d} = \mathbf{G_1 m} + \mathbf{G_2}[(\mathbf{Qm}) \circ (\mathbf{Qm})],$$

where $\mathbf{P}$ represents the instantaneous phase of the seismic data. For details of the definition of equation $\mathbf{d} = \mathbf{G_1 m} + \mathbf{G_2}[(\mathbf{Qm}) \circ (\mathbf{Qm})]$, please read Appendix A.

Then, $\widehat{\mathbf{d}} = \text{Hilbert}(\mathbf{d})$ can be rewritten as:

$$
\begin{aligned}
\widehat{\mathbf{d}} &= \text{Hilbert}(\mathbf{G_1 m} + \mathbf{G_2}[(\mathbf{Qm}) \circ (\mathbf{Qm})] + \mathbf{N}) \\
&= \text{Hilbert}(\mathbf{G_1})\mathbf{m} + \text{Hilbert}(\mathbf{G_2})[(\mathbf{Qm}) \circ (\mathbf{Qm})] + \widehat{\mathbf{N}} \\
&= \mathbf{G}_{\text{H1}} \mathbf{m} + \mathbf{G}_{\text{H2}}[(\mathbf{Qm}) \circ (\mathbf{Qm})] + \widehat{\mathbf{N}},
\end{aligned}
\tag{13}
$$

with

$$
\mathbf{G}_{\text{H1}} = \frac{1}{2}
\begin{bmatrix}
\mathbf{C}_1(\alpha_1)\mathscr{H}(\mathbf{W}_1) & \mathbf{C}_2(\alpha_1)\mathscr{H}(\mathbf{W}_1) & \mathbf{C}_3(\alpha_1)\mathscr{H}(\mathbf{W}_1) \\
\mathbf{C}_1(\alpha_2)\mathscr{H}(\mathbf{W}_2) & \mathbf{C}_2(\alpha_2)\mathscr{H}(\mathbf{W}_2) & \mathbf{C}_3(\alpha_2)\mathscr{H}(\mathbf{W}_2) \\
\vdots & \vdots & \vdots \\
\mathbf{C}_1(\alpha_k)\mathscr{H}(\mathbf{W}_k) & \mathbf{C}_2(\alpha_k)\mathscr{H}(\mathbf{W}_k) & \mathbf{C}_3(\alpha_k)\mathscr{H}(\mathbf{W}_k)
\end{bmatrix}
\mathbf{D},
$$

$$
\mathbf{G}_{\text{H2}} =
\begin{bmatrix}
\mathbf{C}_4(\alpha_1)\mathscr{H}(\mathbf{W}_1) & \mathbf{C}_5(\alpha_1)\mathscr{H}(\mathbf{W}_1) & \mathbf{C}_6(\alpha_1)\mathscr{H}(\mathbf{W}_1) \\
\mathbf{C}_4(\alpha_2)\mathscr{H}(\mathbf{W}_2) & \mathbf{C}_5(\alpha_2)\mathscr{H}(\mathbf{W}_2) & \mathbf{C}_6(\alpha_2)\mathscr{H}(\mathbf{W}_2) \\
\vdots & \vdots & \vdots \\
\mathbf{C}_4(\alpha_k)\mathscr{H}(\mathbf{W}_k) & \mathbf{C}_5(\alpha_k)\mathscr{H}(\mathbf{W}_k) & \mathbf{C}_6(\alpha_k)\mathscr{H}(\mathbf{W}_k)
\end{bmatrix},
$$

where $\mathbf{G}_{\text{H1}}$ and $\mathbf{G}_{\text{H2}}$ are the Hilbert transform matrix of the forward operators $\mathbf{G}_1$ and $\mathbf{G}_2$ respectively. $\text{Hilbert}(\mathbf{W}_i)$ is abbreviated as $\mathscr{H}(\mathbf{W}_i)$. $\mathbf{N}$ represents the seismic noise.

In order to verify the reliability of Eq. (13), we carried out noise-free seismic data synthesis based on the second-order equation derived from Section 2.1. The dominant frequency of the Ricker wavelet is taken as 35 Hz, the sampling interval is 2 ms, and the range of the incidence angle is 5°–45°. Fig. 1 shows the synthesized seismic data and the Hilbert transform curve at an incidence angle of 30°. The black curve represents the noise-free synthetic seismic data, the blue curve represents the Hilbert transform curve calculated by the equation $\widehat{\mathbf{d}} = \text{Hilbert}(\mathbf{G_1 m} + \mathbf{G_2}[(\mathbf{Qm}) \circ (\mathbf{Qm})])$, and the red curve represents the Hilbert transform curve calculated by the equation $\widehat{\mathbf{d}} = \mathbf{G}_{\text{H1}} \mathbf{m} + \mathbf{G}_{\text{H2}}[(\mathbf{Qm}) \circ (\mathbf{Qm})]$. By comparing the red and blue curves, it can be seen that the two curves are consistent, which proves the reliability of Eq. (13).

By simplifying Eq. (12), the constraint term for the instantaneous phase is expressed as follows:

$$
\begin{aligned}
\mathbf{D}_{\text{SH}} &= \mathbf{D}_{\text{SH1}} + \mathbf{D}_{\text{SH2}} \\
&=
\begin{bmatrix}
1./\mathbf{d}(\alpha_1) & & \\
& \ddots & \\
& & 1./\mathbf{d}(\alpha_k)
\end{bmatrix}
\mathbf{G}_{\text{H1}} \mathbf{m} \\
&+
\begin{bmatrix}
1./\mathbf{d}(\alpha_1) & & \\
& \ddots & \\
& & 1./\mathbf{d}(\alpha_k)
\end{bmatrix}
\mathbf{G}_{\text{H2}}[(\mathbf{Qm}) \circ (\mathbf{Qm})] \\
&= \text{Diag}[1./\mathbf{d}]\mathbf{G}_{\text{H1}} \mathbf{m} + \text{Diag}[1./\mathbf{d}]\mathbf{G}_{\text{H2}}[(\mathbf{Qm}) \circ (\mathbf{Qm})] \\
&= \mathbf{G}_{\text{SH1}} \mathbf{m} + \mathbf{G}_{\text{SH2}}[(\mathbf{Qm}) \circ (\mathbf{Qm})] \\
&= \tan(\mathbf{P})
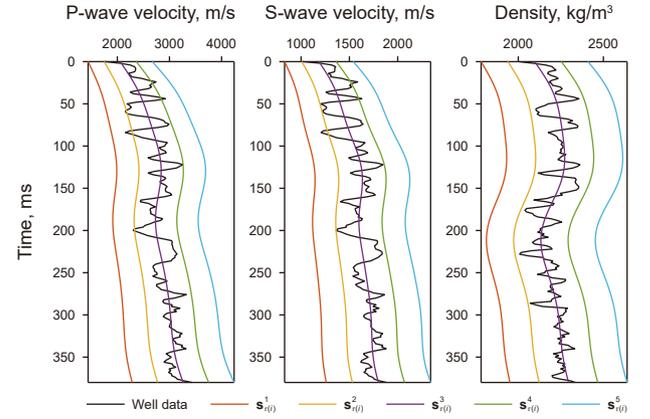\end{aligned}
\tag{14}
$$

Fig. 3. Theoretical well data and prior support points.

where $\mathbf{D}_{\text{SH}}$ represents the constraint term for the instantaneous phase of seismic trace, and Diag represents diagonal matrix.

To verify the plausibility of Eq. (14), we show in Fig. 2 a comparison of the instantaneous phase constraint terms for an incidence angle of 30°. The black curve is calculated from equation $\tan(\mathbf{P})$, and the red curve is calculated from equation $\mathbf{G}_{\text{SH1}} \mathbf{m} + \mathbf{G}_{\text{SH2}}[(\mathbf{Qm}) \circ (\mathbf{Qm})]$. Fig. 2 further validates and highlights that the instantaneous phase information of seismic signals exhibits heightened sensitivity to subsurface thin-layer structures and medium variations.

The solution of the AVO inversion objective function based on higher order approximation and instantaneous phase constraints can be written as:

$$
\begin{aligned}
f(\mathbf{m}) = &\min_{\mathbf{m}} \|\mathbf{d} - \mathbf{G}_1 \mathbf{m} - \mathbf{G}_2((\mathbf{Qm}) \circ (\mathbf{Qm}))\|_2^2 \\
&+ \min_{\mathbf{m}} \|\mathbf{D}_{\text{SH}} - \mathbf{G}_{\text{SH1}} \mathbf{m} - \mathbf{G}_{\text{SH1}}((\mathbf{Qm}) \circ (\mathbf{Qm}))\|_2^2.
\end{aligned}
\tag{15}
$$

A simplification of Eq. (15) can be expressed as:

$$
f(\mathbf{m}) = \min_{\mathbf{m}} \|\mathbf{d} - \mathbf{Gm}\|_2^2 + \min_{\mathbf{m}} \|\mathbf{D}_{\text{SH}} - \mathbf{G}_{\text{SH}} \mathbf{m}\|_2^2,
\tag{16}
$$

with

$$\mathbf{Gm} = \mathbf{G}_1 \mathbf{m} + \mathbf{G}_2((\mathbf{Qm}) \circ (\mathbf{Qm})),$$

$$\mathbf{G}_{\text{SH}} \mathbf{m} = \mathbf{G}_{\text{SH1}} \mathbf{m} + \mathbf{G}_{\text{SH1}}((\mathbf{Qm}) \circ (\mathbf{Qm})).$$
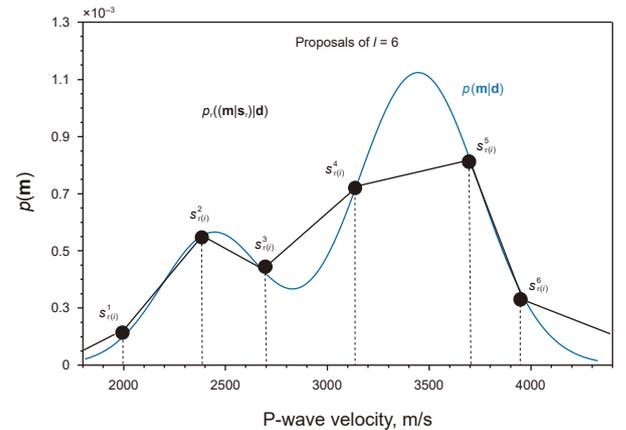

Fig. 4. Piecewise linear function of proposals.

2.3. Improved probabilistic seismic AVO inversion using the improved IA2RMS-Gibbs algorithm

In order to efficiently obtain the optimal solution of Eq. (16), while avoiding the problem of integral operations, which is difficult to solve in the Bayesian algorithm, we propose an improved IA2RMS-Gibbs algorithm (Martino et al., 2015; Li et al., 2022a,b; Zuo et al., 2024) to address this problem.

The probabilistic solution of the inverse problem is the posterior probability density function (PDF). The posterior probability density function $p(\mathbf{m}|\mathbf{d})$ can be obtained by combining the likelihood function $p(\mathbf{d}|\mathbf{m})$ and the prior probability density function $p(\mathbf{m})$ under the Bayesian framework (Grana, 2022):

$$p(\mathbf{m}|\mathbf{d}) = \frac{p(\mathbf{d}|\mathbf{m})p(\mathbf{m})}{p(\mathbf{d})} \tag{17}$$

where $p(\mathbf{d})$ is a constant and generally set to an appropriate value according to the actual situation.

A priori information can be obtained from elastic parameters on logs. It is generally assumed that the prior information obeys a Gaussian distribution, the mean matrix of $\mathbf{m}$ is $\boldsymbol{\mu}_{\mathrm{m}}$, and the standard deviation is σ_{m}, the prior probability density function can be written as:

$$p(\mathbf{m}) = \frac{1}{\left(2\pi\sigma_{\mathrm{m}}^2\right)^{\frac{N}{2}}} \exp\left\{-\frac{\|\mathbf{m} - \boldsymbol{\mu}_{\mathrm{m}}\|^2}{2\sigma_{\mathrm{m}}^2}\right\} \tag{18}$$

where N represents the number of seismic data sampling points.

Combining the quadratic approximation equation derived in Eq. (16) with the instantaneous phase constraint term, the likelihood function in the Bayesian framework is expressed as follows:

$$p(\mathbf{d}|\mathbf{m}) = \frac{1}{\left(2\pi\sigma_d^2\right)^{\frac{N}{2}}} \exp\left\{-\frac{\|\mathbf{d} - \mathbf{Gm}\|^2}{2\sigma_d^2}\right\} \cdot \frac{1}{\left(2\pi\sigma_{\mathrm{sh}}^2\right)^{\frac{N}{2}}}$$
$$\exp\left\{-\frac{\|\mathbf{D}_{\mathrm{SH}} - \mathbf{G}_{\mathrm{SH}}\mathbf{m}\|^2}{2\sigma_{\mathrm{sh}}^2}\right\} \tag{19}$$

where σ serves as a damping factor correlated with the signal-to-noise ratio (SNR).

The posterior probability density function is written as follows:

$$p(\mathbf{m}|\mathbf{d}) = \exp(\log(p(\mathbf{d}|\mathbf{m})) + \log(p(\mathbf{m})))$$
$$= \exp\left(-\frac{\|\mathbf{d} - \mathbf{Gm}\|^2}{2\sigma_d^2} - \frac{\|\mathbf{D}_{\mathrm{SH}} - \mathbf{G}_{\mathrm{SH}}\mathbf{m}\|^2}{2\sigma_{\mathrm{sh}}^2} - \frac{\|\mathbf{m} - \boldsymbol{\mu}_{\mathrm{m}}\|^2}{2\sigma_{\mathrm{m}}^2}\right) \tag{20}$$

The Gibbs sampling algorithm has the advantage of producing a range of adaptive proposal distributions, and the IA2RMS

algorithm has the advantage of improving the stability of Markov chains. In order to efficiently perform an iterative inversion of the posterior PDF derived from Eq. (20), we combined the Gibbs sampling and IA2RMS algorithms. It is worth noting that the interpolation method used in our improved Gibbs sampling is the first-order Taylor approximation.

The proposed IA2RMS-Gibbs algorithm has two important parameters, the number of iterations of the Markov chain and the number of iterations of the algorithm. At the beginning of the algorithm, we set both the number of iterations of the Markov chain k and the number of algorithm iterations τ to zero.

A series of support points (Fig. 3) were obtained by linear interpolation of the low-frequency model $\mathbf{m}_0$, and its expression is

$$\mathbf{S}_\tau = \left\{\mathbf{s}_{\tau(i)}^1, \mathbf{s}_{\tau(i)}^2, \cdots, \mathbf{s}_{\tau(i)}^l\right\} \tag{21}$$

where l represent the number of support points, and $s_{\tau(i)}^1 < s_{\tau(i)}^2 < \cdots < s_{\tau(i)}^l$, i represent the location of model $\mathbf{m}_0$, $i = 1, 2, \ldots, N$.

Building proposals $p_\tau((\mathbf{m}|\mathbf{S}_\tau)|\mathbf{d})$ from a set of support points $\mathbf{S}_\tau$ using a piecewise linear function (Fig. 4), which can be expressed as

$$p_\tau((\mathbf{m}|\mathbf{S}_\tau)|\mathbf{d}) = \begin{cases} \eta_0 s + p_{\tau(i)}^1((\mathbf{m}|\mathbf{S}_\tau)|\mathbf{d}) - \eta_0 s_{\tau(i)}^1, & s \in \left(0, s_{\tau(i)}^1\right] \\ L_{l,l+1}, & s \in \left(s_{\tau(i)}^l, s_{\tau(i)}^{l+1}\right] \\ \eta_l s + p_{\tau(i)}^l((\mathbf{m}|\mathbf{S}_\tau)|\mathbf{d}) - \eta_l s_{\tau(i)}^l, & s \in \left(s_{\tau(i)}^l, +\infty\right] \end{cases} \tag{22}$$

where η_0 and η_l represent the approximated slopes of line segments between support points $s_{\tau(i)}^1$ to $s_{\tau(i)}^2$ and $s_{\tau(i)}^{l-1}$ to $s_{\tau(i)}^l$, respectively. Within the interval $(s_{\tau(i)}^l, s_{\tau(i)}^{l+1}]$, $L_{l,l+1}$ represents a piecewise linear interpolation function constructed by connecting the support points $s_{\tau(i)}^l$ and $s_{\tau(i)}^{l+1}$. $p_{\tau(i)}^l((\mathbf{m}|\mathbf{S}_\tau)|\mathbf{d})$ represents the posterior probability density of the model parameter $\mathbf{m}$ evaluated at the designated support point $s_{\tau(i)}^l$. s is obtained by applying a first-order Taylor interpolation approximation method to interpolate a series of support points. This approach constructs a continuous linear approximation between adjacent points through the first-order term of local Taylor series expansion.

It is independent of the current state of the chain for $p_\tau((\mathbf{m}|\mathbf{S}_\tau)|\mathbf{d})$, which means that the proposal tends to converge to posterior PDF. And when a new proposal enters the rejection loop in the IA2RMS algorithm, the new support points show a tendency to change, first increasing and then decreasing to zero. Algorithm 1 shows the pseudo-code of the proposed algorithm of IA2RMS-Gibbs.

Algorithm 1.   Improved algorithm of IA2RMS-Gibbs

---

1) **Initialization:** set $k=0$ (The number of chain iteration), $\tau=0$ (The number of algorithm iteration), a series of support points $\mathbf{S}_\tau$ were obtained by linear interpolation of the low-frequency model $\mathbf{m}_0$, where $\mathbf{S}_\tau=\left\{\mathbf{s}^1_{\tau(i)},\mathbf{s}^2_{\tau(i)},\cdots,\mathbf{s}^l_{\tau(i)}\right\}$, l represent the number of support points and $s^1_{\tau(i)}<s^2_{\tau(i)}<\cdots<s^l_{\tau(i)}$, $i=1,2,...,N$.

Iterations (while $k<K$):

2)   Building proposals from a set of support points $\mathbf{S}_\tau$ using an improved Gibbs sampling algorithm, which can be expressed as $p_\tau\big((\mathbf{m}|\mathbf{S}_\tau)|\mathbf{d}\big)$.

3)   Draw $\mathbf{m}'\sim\tilde{p}_\tau\big((\mathbf{m}|\mathbf{S}_\tau)|\mathbf{d}\big)\propto p_\tau\big((\mathbf{m}|\mathbf{S}_\tau)|\mathbf{d}\big)$ and set $u_1\sim U\big([0,1]\big)$.

4)   If $u_1>\dfrac{p(\mathbf{m}'|\mathbf{d})}{p\big((\mathbf{m}'|\mathbf{S}_\tau)|\mathbf{d}\big)}$, then reject $\mathbf{m}'$, set $\mathbf{S}_{\tau+1}=\mathbf{S}_\tau\bigcup\{\mathbf{m}'\}$,

update $\tau=\tau+1$ and go back to step 2.

5)   Otherwise, if $u_1\leq\dfrac{p(\mathbf{m}'|\mathbf{d})}{p\big((\mathbf{m}'|\mathbf{S}_\tau)|\mathbf{d}\big)}$, set $u_2\sim U\big([0,1]\big)$, then the acceptance probability Ω can be expressed as:

$$\Omega=\min\left[1,\frac{p(\mathbf{m}'|\mathbf{d})\min\big[p(\mathbf{m}_k|\mathbf{d}),p\big((\mathbf{m}_k|\mathbf{S}_\tau)|\mathbf{d}\big)\big]}{p(\mathbf{m}_k|\mathbf{d})\min\big[p(\mathbf{m}'|\mathbf{d}),p\big((\mathbf{m}'|\mathbf{S}_\tau)|\mathbf{d}\big)\big]}\right],\text{ if}$$

$u_2\leq\Omega$, then accept $\mathbf{m}'$ and update $\mathbf{m}_{k+1}=\mathbf{m}'$, $\mathbf{m}_{\text{aux}}=\mathbf{m}_k$.

6)   Otherwise, if $u_2>\Omega$, reject $\mathbf{m}'$, and set $\mathbf{m}_{k+1}=\mathbf{m}_k$, $\mathbf{m}_{\text{aux}}=\mathbf{m}'$.

7) Draw $u_3\sim U\big([0,1]\big)$, if $u_3>\dfrac{p\big((\mathbf{m}_{\text{aux}}|\mathbf{S}_\tau)|\mathbf{d}\big)}{p(\mathbf{m}_{\text{aux}}|\mathbf{d})}$, then set $\mathbf{S}_{\tau+1}=\mathbf{S}_\tau\bigcup\{\mathbf{m}_{\text{aux}}\}$.Otherwise, set $\mathbf{S}_{\tau+1}=\mathbf{S}_\tau$.

8) Update $k=k+1$, $\tau=\tau+1$ and return to step 2.

---

3. Examples

3.1. Model experiment

The accuracy of reflection coefficients plays a crucial role in seismic inversion, and accurate reflection coefficients can effectively reduce the multiplicity of solutions in the inversion. In order to test the accuracy of our derived second-order approximation equation for PP wave reflectivity, we use a typical AVO model interface for validation. The parameters of the model interface are derived from actual well data in a study area, and the specific parameter settings are shown in Table 1. Meanwhile, we compare the accuracy of Zoeppritz, Ruger approximation (Rüger, 1997, 2002), and Wang approximation (Wang, 1999) (shown in Fig. 5). Compared with Rüger's linear approximation, the quadratic approximation introduces second-order terms of density and elastic parameters, which substantially improves the accuracy of the reflection coefficient. Comparative analysis of four typical AVO interfaces demonstrates that Rüger's linear approximation, Wang's approximation, and the quadratic approximation exhibit equivalent accuracy to the exact equation at near angles (<30°). Notably, the quadratic approximation (red dotted curves) shows enhanced convergence with the exact solution (black curves) at far angles (>30°), confirming the superior performance of our derived second-order approximation in large-angle scenarios. The integration of Class IV data from Table 1 with Fig. 5(d) collectively demonstrates that the proposed second-order approximation achieves closer alignment with the exact Zoeppritz reflection coefficients when abrupt variations in elastic parameters occur (e.g., at high-velocity/low-velocity layer interfaces). This provides robust evidence for the method's enhanced fidelity in resolving sharp lithological contrasts compared to conventional linear approximations.

The forward operator is constructed from the derived quadratic PP reflection approximation and instantaneous phase constraint term, and then the probabilistic AVO inversion is carried out using the improved IA2RMS algorithm with Gibbs sampling, and the feasibility and noise immunity of the method are verified using field logging data. Meanwhile, the inversion results and uncertainty analysis results of the conventional stochastic inversion and the proposed inversion method are compared. By the way, the conventional stochastic inversion method covered in this paper refers to the IA2RMS stochastic inversion under the Ruger approximation formulation. The synthesis of seismic data was performed using the derived quadratic PP reflection approximation, where the dominant frequency of the Ricker wavelet is taken as 35 Hz, the sampling interval is 2 ms, and the range of the incidence angle is 5°–45°. Fig. 6 shows the synthesized seismic data, (a) noise-free seismic data, (b) seismic data with SNR = 9:1, (c) seismic data with SNR = 2:1, and (d) seismic data with

Table 1
The typical interface model of different class AVO. Parameters are obtained from well logs in the study data.

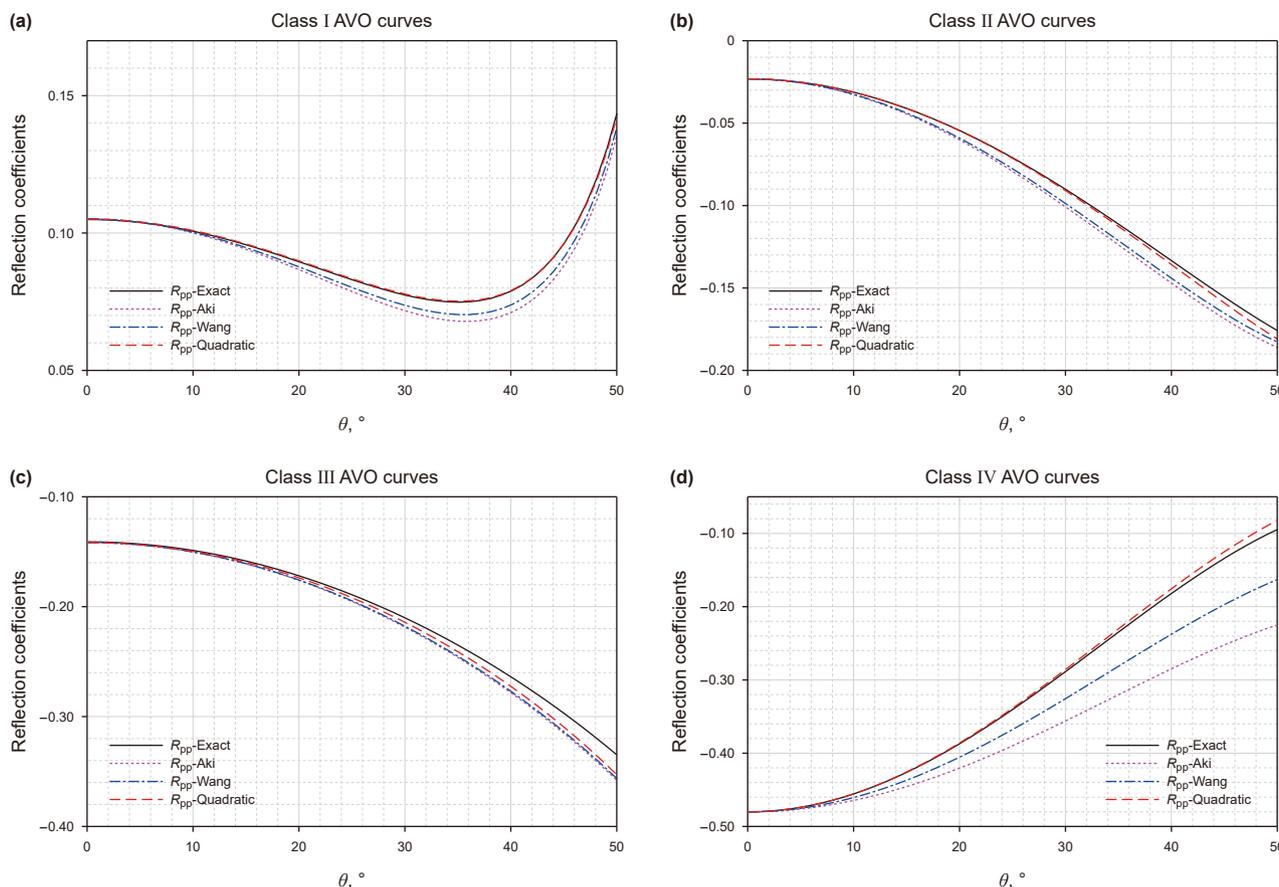| AVO class	Geology	V_p, m/s	V_s, m/s	ρ, g/cm³
Class I	Upper medium	2545	1255	2.30
	Lower medium	2985	1530	2.42
Class II	Upper medium	2655	1180	2.29
	Lower medium	2790	1675	2.08
Class III	Upper medium	3005	1285	2.30
	Lower medium	2455	1655	2.12
Class IV	Upper medium	3655	2095	2.33
	Lower medium	2285	1065	1.40

Fig. 5. Comparison of reflection coefficients of four approximate formulas for different AVO types: **(a)** Class I, **(b)** Class II, **(c)** Class III, **(d)** Class IV. The black curve represents the result obtained from the Zoeppritz, the pink dotted curves represent the results obtained by the Ruger approximation equation (Rüger, 1997, 2002), the blue dotted curve represents the result of Wang approximation formula (Wang, 1999), and the red dotted curve represents the result of second-order approximation formula.
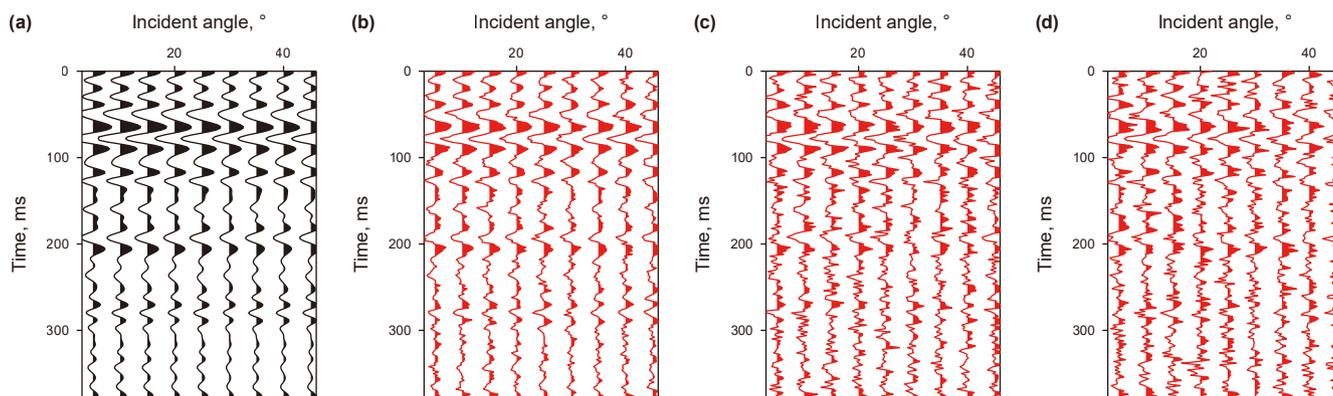
Fig. 6. Results of synthetic seismic data obtained from the proposed second-order approximation. **(a)** Noise-free seismic data, **(b)** seismic data with SNR = 9:1, **(c)** seismic data with SNR = 5:1, and **(d)** seismic data with SNR = 1:1.

SNR = 1:1. Figs. 7–10 show the comparison of the inversion results for noise-free, SNR = 9:1, SNR = 2:1, and SNR = 1:1, respectively. Comparison of the inversion results of P-wave velocity (V_p), S-wave velocity (V_s) and density (ρ) in Figs. 7–10 demonstrates the high accuracy of the proposed probabilistic AVO inversion method over the conventional stochastic inversion method. It is worth mentioning that both stochastic inversion methods show strong noise immunity, which verifies the feasibility and noise immunity of the proposed inversion method.

In order to show the accuracy of the inversion results of the two inversion methods more clearly, Fig. 11 demonstrates the histograms of the two inversion methods compared with the actual model. Fig. 11(a)–(c) show the comparison of the conventional stochastic inversion results of P-wave velocity, S-wave velocity, and density with the histograms of the actual model, and Fig. 11 (d)–(f) show the comparison of the proposed probabilistic AVO inversion results of P-wave velocity, S-wave velocity, and density with the histograms of the actual model, respectively. The
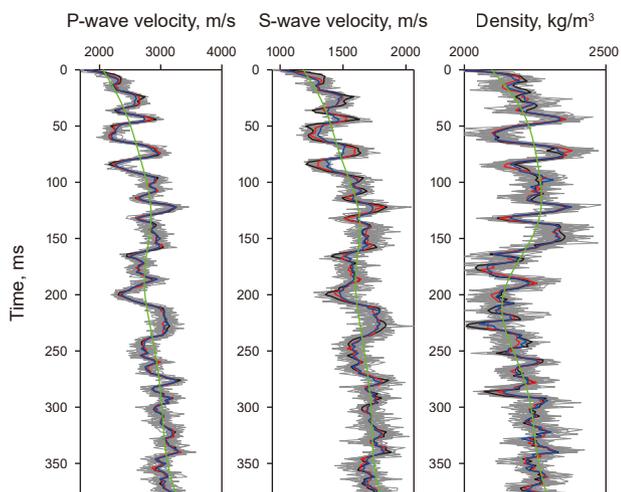
Fig. 7. Noise-free AVO inversion results of P-wave velocity, S-wave velocity, and density. The black curve represents the actual model data, the green curve represents the low-frequency model, the grey curve represents the results of 20 stochastic inversions, the blue curve represents the stochastic inversion results obtained by the traditional method, and the red curve represents the stochastic inversion results obtained by the method proposed in this paper.
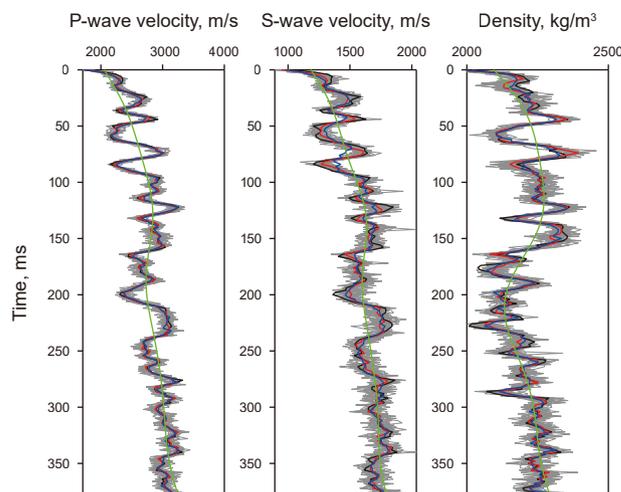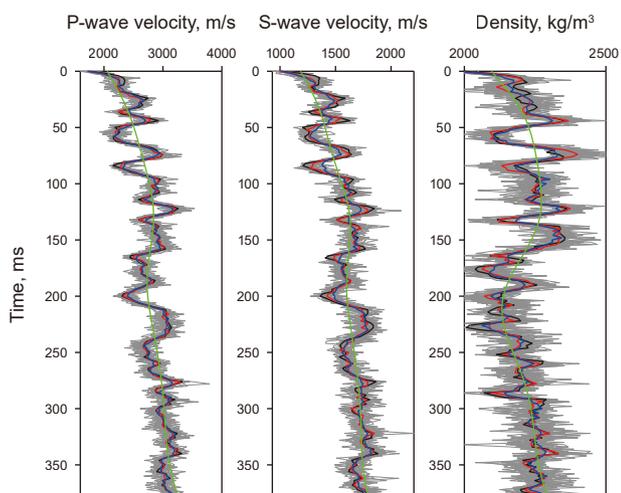

Fig. 9. AVO inversion results of P-wave velocity, S-wave velocity, and density for SNR = 2:1. The black curve represents the actual model data, the green curve represents the low-frequency model, the grey curve represents the results of 20 stochastic inversions, the blue curve represents the stochastic inversion results obtained by the traditional method, and the red curve represents the stochastic inversion results obtained by the method proposed in this paper.

Fig. 8. AVO inversion results of P-wave velocity, S-wave velocity, and density for SNR = 9:1. The black curve represents the actual model data, the green curve represents the low-frequency model, the grey curve represents the results of 20 stochastic inversions, the blue curve represents the stochastic inversion results obtained by the traditional method, and the red curve represents the stochastic inversion results obtained by the method proposed in this paper.
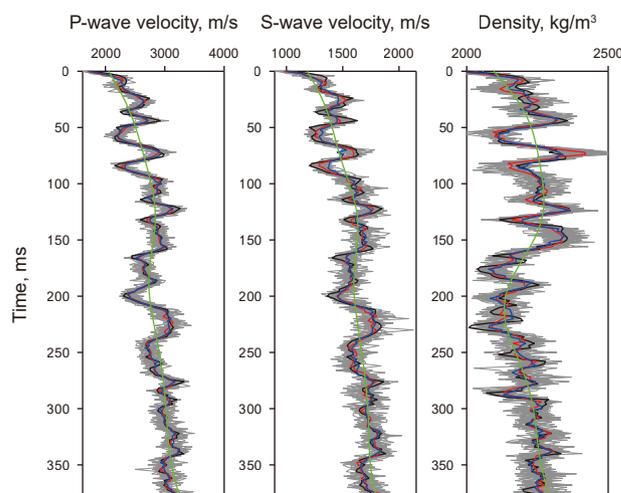

Fig. 10. AVO inversion results of P-wave velocity, S-wave velocity, and density for SNR = 1:1. The black curve represents the actual model data, the green curve represents the low-frequency model, the grey curve represents the results of 20 stochastic inversions, the blue curve represents the stochastic inversion results obtained by the traditional method, and the red curve represents the stochastic inversion results obtained by the method proposed in this paper.

histogram comparison of the two methods illustrates that the proposed probabilistic AVO inversion method has higher accuracy, moreover, its inversion results are closer to the actual model and less affected by seismic noise. Fig. 12 shows the uncertainty analysis of the 20 inversion results for both the conventional stochastic inversion method and the proposed probabilistic AVO inversion method. In the legend, black circles denote true model values, blue circles indicate conventional inversion results, and red circles represent outputs from the proposed stochastic method. Fig. 12(a)–(c) show the uncertainty analysis of the conventional P-wave velocity, S-wave velocity, and density stochastic inversion results, and Fig. 12(d)–(f) show the uncertainty analysis of the proposed P-wave velocity, S-wave velocity, and density stochastic inversion results, respectively. The comparison of the uncertainty

assessment of the two stochastic inversion methods demonstrates that the proposed probabilistic AVO inversion method is more stable with less uncertainty. It is also shown that the proposed inversion method has a much better convergence, which greatly improves the efficiency of the inversion.

To highlight the individual contributions of quadratic approximation, phase constraints, and the improved IA2RMS-Gibbs algorithm, Fig. 13 presents the P-wave velocity convergence curves derived from the averages of 20 Markov chains under a SNR of 1:1. The blue line represents the conventional IA2RMS stochastic inversion, orange represents the stochastic inversion with the improved IA2RMS-Gibbs algorithm, yellow represents the instantaneous phase-constrained stochastic inversion based on the improved IA2RMS-Gibbs algorithm, purple represents the
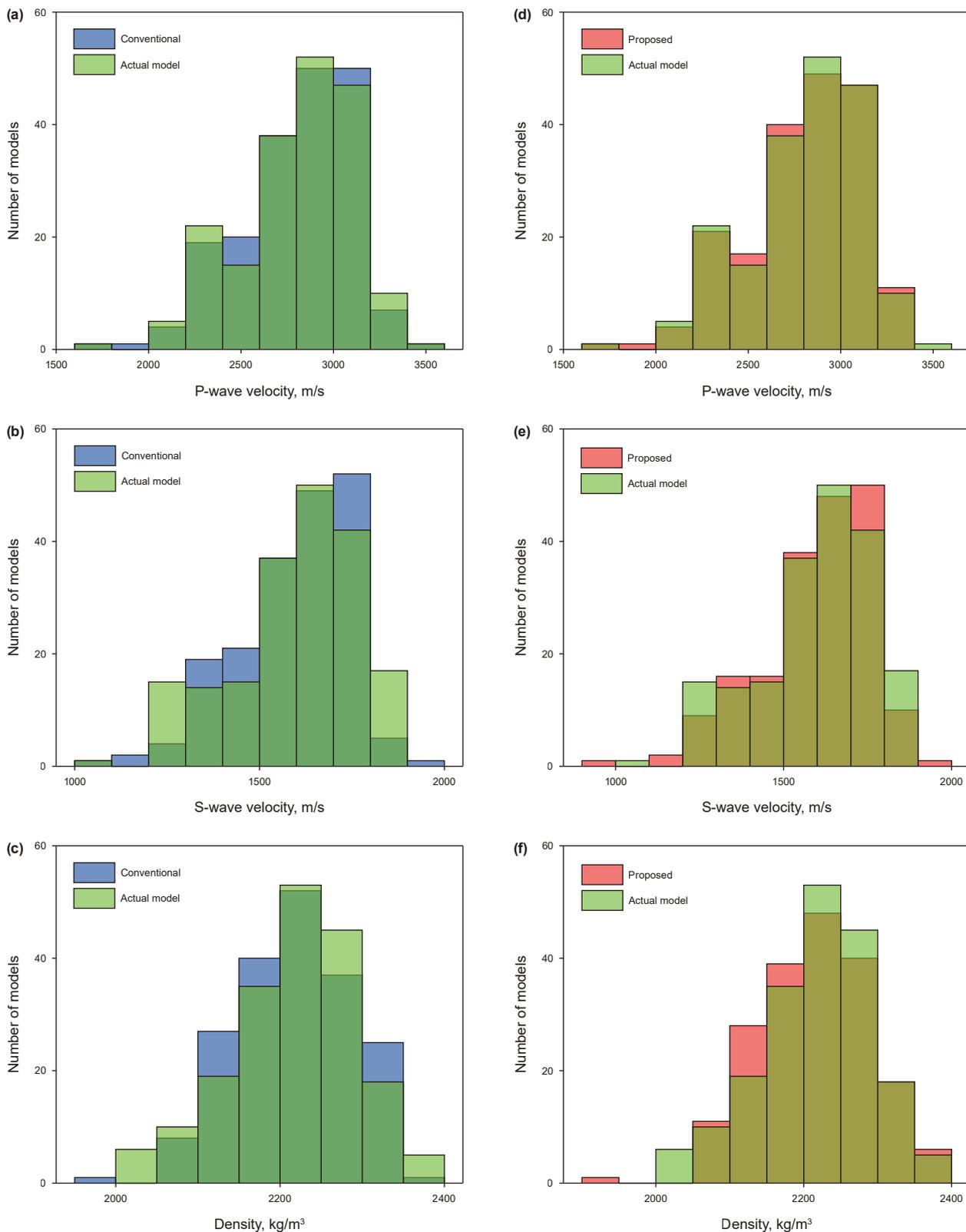
Fig. 11. Comparison of histogram error statistics of noise-free AVO inversion results. The green histogram shows the statistics of the actual model, the blue histogram represents the statistics of the conventional stochastic inversion results, and the red histogram represents the statistics of the proposed stochastic inversion results. **(a)**–**(c)** are conventional stochastic inversion results for P-wave velocity, S-wave velocity, and density, respectively, and **(d)**–**(f)** are the proposed stochastic inversion results for P-wave velocity, S-wave velocity, and density, respectively.
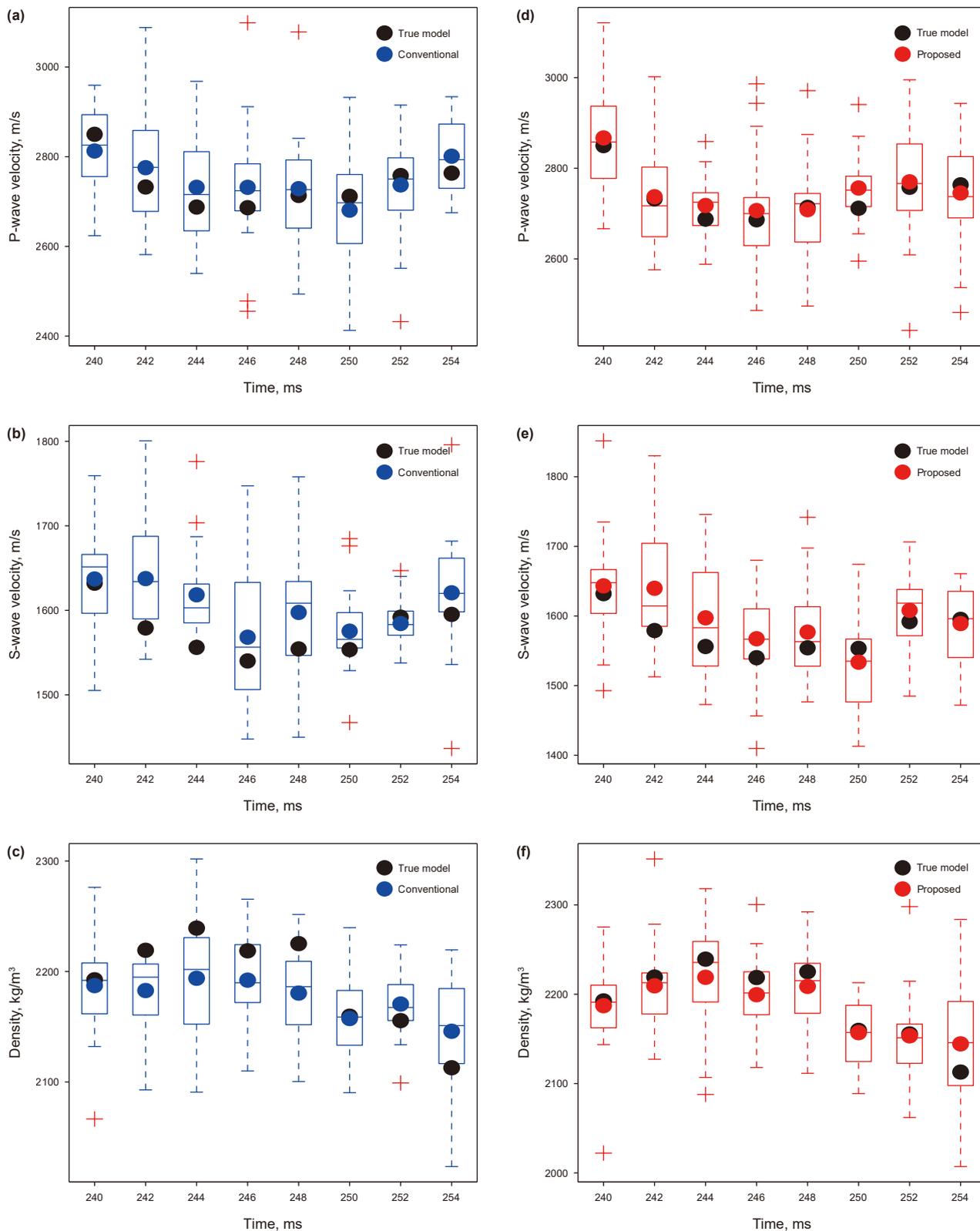
Fig. 12. Uncertainty analysis of inversion results. Black circles represent the values of the true model, blue circles represent the results of the conventional inversion, and red represents the results of the proposed stochastic inversion. **(a)–(c)** are the uncertainty analyses of the conventional stochastic inversion results for the P-wave velocity, the S-wave velocity, and the density, respectively, and **(d)–(f)** are the uncertainty analyses of the proposed stochastic inversion results for the P-wave velocity, the S-wave velocity, and the density, respectively.
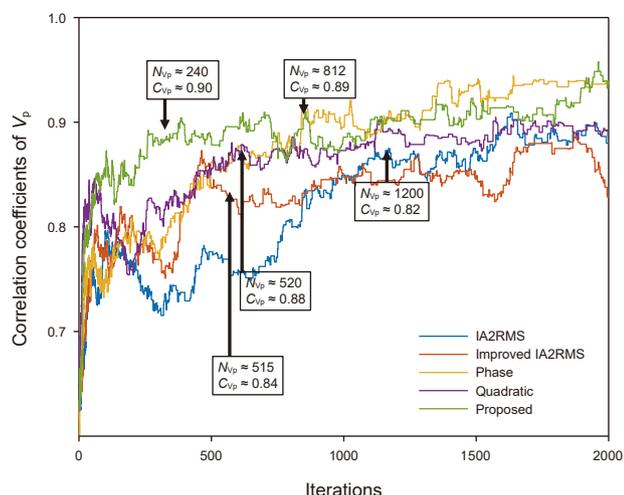
Fig. 13. Convergence curves of P-wave velocities derived from averages of 20 Markov chains under SNR = 1:1. The blue line represents the conventional IA2RMS stochastic inversion, orange represents the stochastic inversion with the improved IA2RMS algorithm, yellow represents the instantaneous phase-constrained stochastic inversion based on the improved IA2RMS algorithm, purple represents the quadratic approximate stochastic inversion based on the improved IA2RMS algorithm, and green represents the proposed inversion method.

Fig. 14. Field angle-stack seismic profiles across well 1. **(a)** Near angle-stack seismic, **(b)** medium angle-stack seismic, and **(c)** far angle-stack seismic.

quadratic approximate stochastic inversion based on the improved IA2RMS-Gibbs algorithm, and green represents improved probabilistic seismic AVO inversion constrained by instantaneous phase using quadratic PP-reflectivity approximation and IA2RMS-Gibbs algorithm. N_{Vp} and C_{Vp} denote the iteration count of the Markov chains and the Pearson correlation coefficient between the inversion results and the P-wave velocity derived from logging data, respectively. A comparative analysis of the blue and orange Markov chain convergence profiles reveals a pronounced divergence in convergence behavior: at an equivalent Pearson correlation coefficient threshold of 0.82, the required iteration counts are 1200 and 515, respectively. This empirically validates that the improved IA2RMS-Gibbs algorithm achieves substantially enhanced convergence rates and computational efficacy compared to conventional methodologies. A comparative analysis of the purple and orange Markov chain convergence profiles demonstrates distinct convergence patterns: the two methodologies require 520 and 515 iterations to achieve stabilization, with correlation coefficient thresholds of 0.88 and 0.84, respectively. These results provide compelling evidence that the quadratic approximation strategy proposed in this study significantly enhances inversion accuracy compared to conventional approaches. A comparative analysis of the yellow and orange Markov chain convergence profiles reveals distinct performance characteristics: the two methodologies require 812 and 515 iterations to achieve stabilization, with correlation coefficient thresholds of 0.89 and 0.84, respectively. While the instantaneous phase-constrained strategy proposed in this study significantly enhances inversion accuracy, its sensitivity to seismic noise introduces non-negligible perturbations to the Markov chains, thereby decelerating convergence rates. To mitigate this limitation, we introduce a novel improved probabilistic seismic AVO inversion constrained by instantaneous phase using quadratic PP-reflectivity approximation and IA2RMS-Gibbs algorithm method. As evidenced by the green convergence profile, the refined methodology attains a correlation coefficient threshold of 0.9 with only 240 iterations, demonstrating simultaneous improvements in both convergence efficiency and inversion precision compared to conventional method.
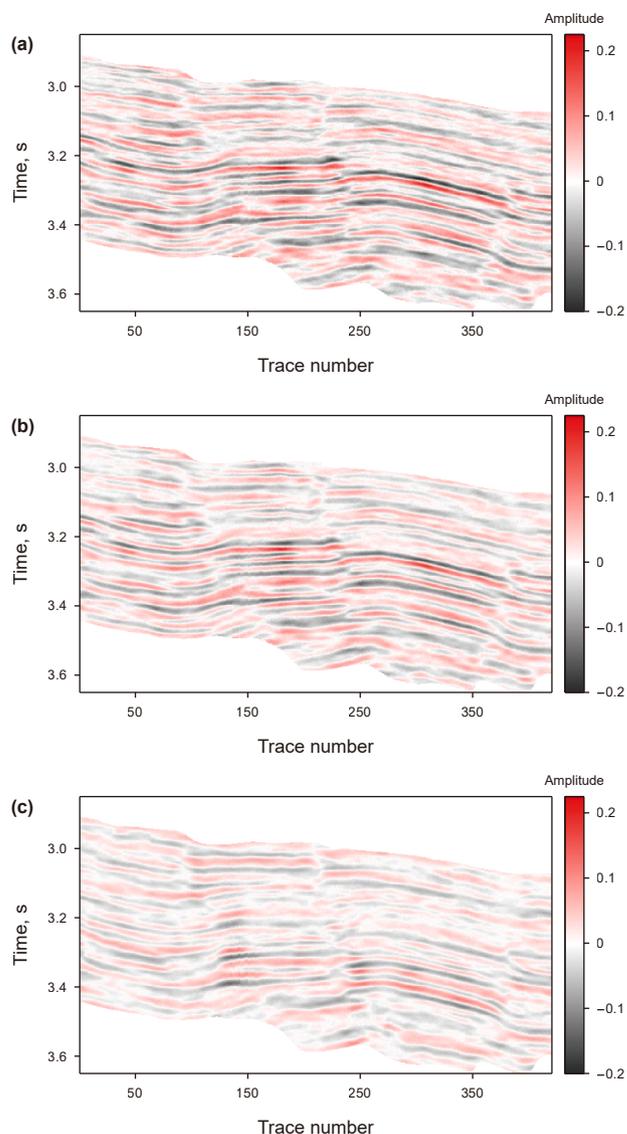
3.2. Field data inversions

To verify the practicality of the proposed inversion method, we applied the method to the field data and at the same time compared the effects of both methods, the conventional stochastic inversion method and the proposed inversion method. Fig. 14 shows the field angle-stack seismic profiles, (a)–(c) for the near angle-stack (4°–18°) seismic, medium angle-stack (14°–28°) seismic and far angle-stack (26°–40°) seismic, respectively. Fig. 15 shows the inversion results of P-wave velocity, S-wave velocity and density obtained by the conventional stochastic inversion method. Fig. 16 shows the inversion results of P-wave velocity, S-wave velocity and density obtained by the proposed probabilistic AVO stochastic inversion method. From the analysis of Figs. 15 and 16, it can be seen that the inversion results of P-wave velocity, S-wave velocity, and density obtained by the two stochastic inversion methods can match the well curves. The comparison of the two stochastic inversion methods illustrates that the proposed probabilistic AVO inversion method has better lateral continuity and higher resolution (indicated by the black arrows in Figs. 15 and
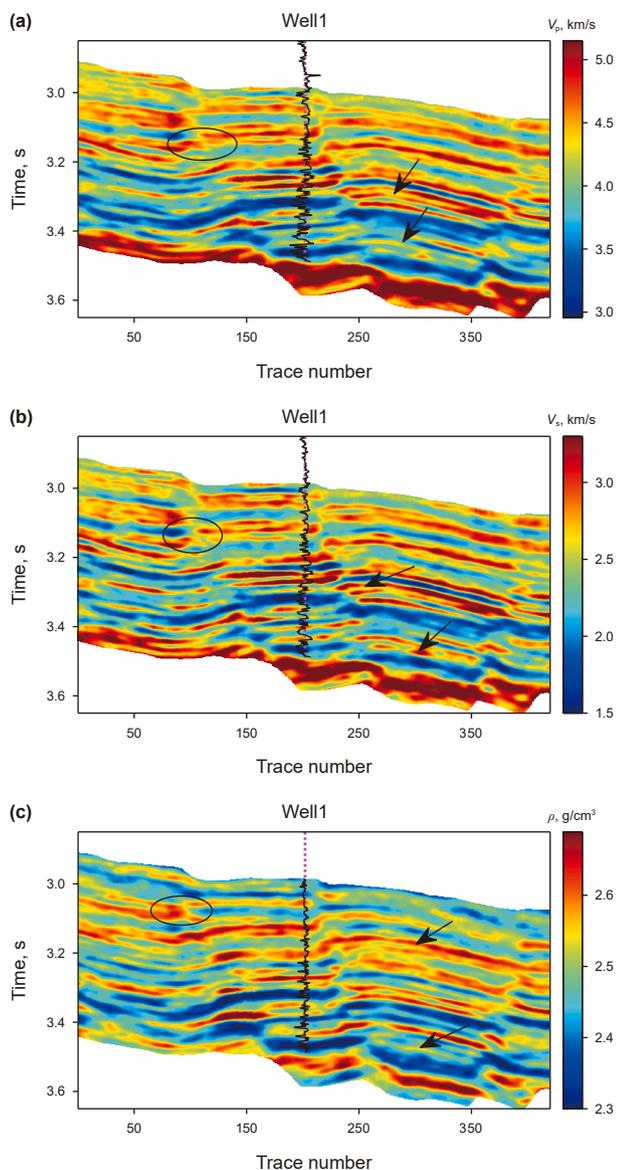
Fig. 15. AVO inversion results cross well 1 obtained by conventional stochastic inversion methods. **(a)** P-wave velocity, **(b)** S-wave velocity, **(c)** density.
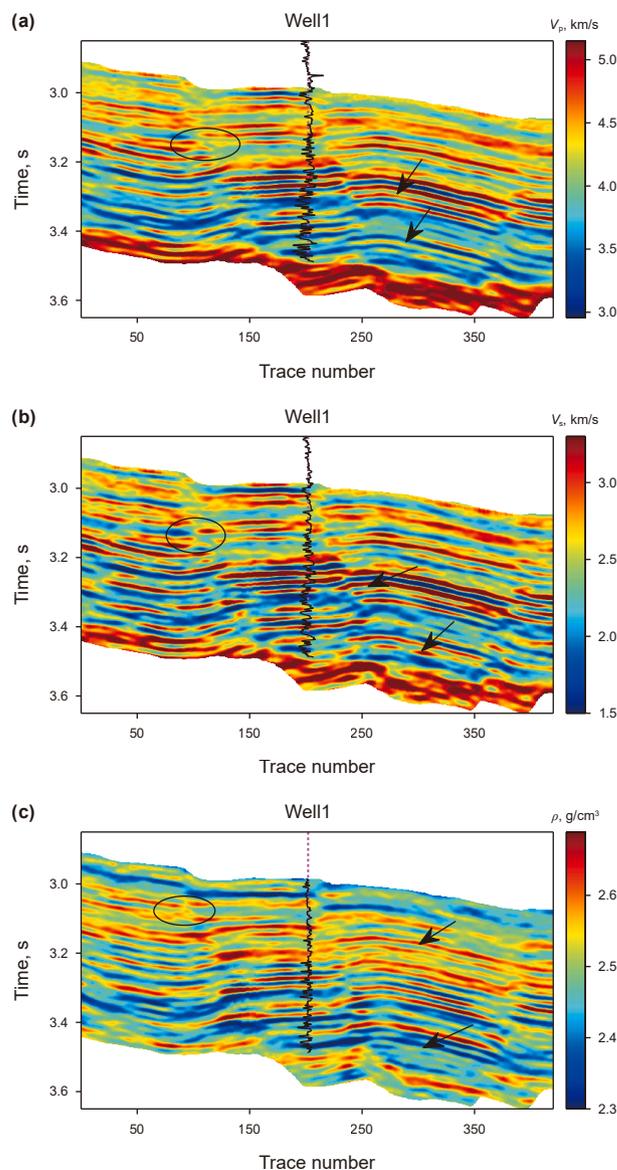

Fig. 16. AVO inversion results cross well 1 obtained by proposed stochastic inversion methods. **(a)** P-wave velocity, **(b)** S-wave velocity, **(c)** density.

16, as an example), and more clearly highlights the stratigraphic interface information (as exemplified by the black ellipse areas in Figs. 15 and 16).

4. Discussion

The IA2RMS-driven probabilistic AVO inversion technique constitutes an advanced nonlinear stochastic approach that formulates an optimized posterior probability density function within a Bayesian inference paradigm. This methodology elegantly circumvents the intractable integration challenges inherent in conventional Bayesian implementations through its multi-chain Markov sampling architecture, while achieving superior vertical resolution compared to deterministic inversion. Despite successful field applications across diverse geological settings, critical challenges persist regarding computational bottlenecks in multi-parameter optimization and rigorous quantification of solution space uncertainties.
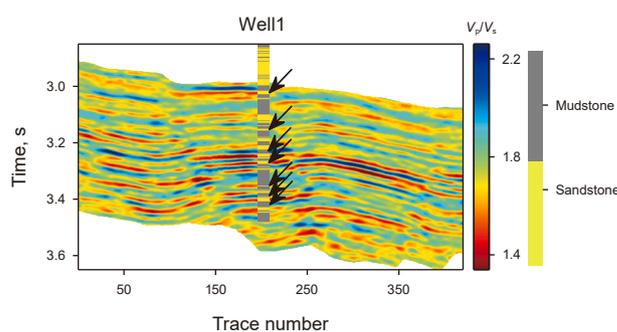

Fig. 17. Estimated elastic parameters cross well 1 obtained by proposed stochastic inversion methods.

In order to reduce the uncertainty of stochastic inversion methods and to improve the accuracy of stochastic inversion. Firstly, this paper derives a new and more accurate quadratic PP

reflection approximation from the PP reflection coefficient equation, By comparing the Ruger linear approximation, the Wang approximation, and the derived quadratic approximation with the exact approximation equations (Fig. 5), it is shown that the quadratic approximation equations have a higher accuracy over a large range of angles. Then, considering the sensitivity of the instantaneous phase to the seismic response, the instantaneous phase constraint term is derived using the Hilbert transform, and the constraint of the instantaneous phase is added to the objective function, which can effectively improve the identification of the stochastic inversion lateral continuity and stratigraphic interface (Fig. 16). Finally, an innovative adaptive AVO stochastic inversion method developed by integrating enhanced Gibbs sampling with the IA2RMS algorithm. This approach enhances the stability of random sampling while ensuring the accuracy of inversion results.

The relative magnitude of the P-wave to S-wave velocity ratio ($V_\mathrm{p}/V_\mathrm{s}$) can effectively distinguish between sandstone and mudstone. The exceptionally low $V_\mathrm{p}/V_\mathrm{s}$ ratio of gas-bearing sandstone serves as a critical indicator in hydrocarbon exploration, while the high $V_\mathrm{p}/V_\mathrm{s}$ ratio of mudstone helps eliminate fluid-related interference. Fig. 17 demonstrates a quantitative lithology comparison between the inverted $V_\mathrm{p}/V_\mathrm{s}$ ratio results and well log data. As illustrated by the inversion results in Fig. 17, the lower and higher $V_\mathrm{p}/V_\mathrm{s}$ values correlate closely with sandstone and mudstone identified (indicated by the black arrows in Fig. 17, as an example) in the well logs, respectively. This further validates that the inversion method proposed in this study can reliably identify hydrocarbon reservoirs.

5. Conclusion

A probabilistic seismic AVO inversion method, using a combination of the quadratic PP reflection approximation and the improved IA2RMS-Gibbs algorithm with the instantaneous phase as a constraint, has been proposed to estimate the elastic parameters of the subsurface medium. In this paper, the derived quadratic approximation equations and instantaneous phase constraint terms are combined and incorporated into the likelihood function in a Bayesian framework, and then the integration of a piecewise linear function strategy with the IA2RMS-Gibbs sampler addresses the inherent limitations of parameter distribution assumptions in stochastic simulations. By strategically incorporating support points within the sampling framework, this hybrid approach enables adaptive refinement of proposal distributions while maintaining Markov chain ergodicity. Finally, the high-dimensional posterior PDFs of the elastic parameters are estimated by a perturbed iterative inversion strategy. The main advantage of the proposed inversion method is that it breaks the limitation of stochastic inversion in the traditional sense, and improves the resolution of the inversion while maintaining a good lateral continuity, which enables the stratigraphic interfaces to be well delineated. The proposed probabilistic AVO inversion method greatly reduces the uncertainty of the stochastic inversion method, which results in a great improvement of the inversion accuracy. Numerical modeling tests and field seismic data also confirm the robustness and feasibility of the proposed probabilistic AVO inversion method.

CRediT authorship contribution statement

Shuang-Shuang Zhou: Writing – review & editing, Validation, Software, Methodology, Data curation, Writing – original draft, Supervision, Resources, Formal analysis, Conceptualization. **Xing-Yao Yin:** Writing – review & editing, Validation, Resources, Visualization, Supervision, Funding acquisition. **Kun Li:** Visualization, Software, Writing – review & editing, Supervision, Methodology. **Ya-Ming Yang:** Visualization, Supervision, Validation.

Declaration of competing interest

We declare that we do not have any commercial or associative interest that represents a conflict of interest in connection with the work submitted.

Acknowledgment

Appendix A. Construction of forward operators

The reflectivity of P-wave velocity, S-wave velocity, and density can be approximated in logarithmic form as

$$R_\mathrm{P}^i = \frac{V_\mathrm{P}^{i+1} - V_\mathrm{P}^i}{V_\mathrm{P}^{i+1} + V_\mathrm{P}^i} \approx \frac{1}{2}\Delta\ln V_\mathrm{P}^i = \frac{1}{2}\left(\ln V_\mathrm{P}^{i+1} - \ln V_\mathrm{P}^i\right),$$

$$R_\mathrm{S}^i = \frac{V_\mathrm{S}^{i+1} - V_\mathrm{S}^i}{V_\mathrm{S}^{i+1} + V_\mathrm{S}^i} \approx \frac{1}{2}\Delta\ln V_\mathrm{S}^i = \frac{1}{2}\left(\ln V_\mathrm{S}^{i+1} - \ln V_\mathrm{S}^i\right),$$

$$R_\rho^i = \frac{\rho^{i+1} - \rho^i}{\rho^{i+1} + \rho^i} \approx \frac{1}{2}\Delta\ln \rho^i = \frac{1}{2}\left(\ln \rho^{i+1} - \ln \rho^i\right), \tag{A.1}$$

where R_P^i, R_S^i, and R_ρ^i are the reflectivity of P- wave, S-wave, density at layer i, respectively. Writing Eq. (A.1) in the form of a matrix can be expressed as:

$$\mathbf{R}_\mathrm{P} \approx \frac{1}{2}\mathbf{D}_1\mathbf{L}_\mathrm{P}, \mathbf{R}_\mathrm{S} \approx \frac{1}{2}\mathbf{D}_1\mathbf{L}_\mathrm{S}, \mathbf{R}_\rho \approx \frac{1}{2}\mathbf{D}_1\mathbf{L}_\rho, \tag{A.2}$$

where $\mathbf{L}_\mathrm{P}$, $\mathbf{L}_\mathrm{S}$, $\mathbf{L}_\rho$ the matrix of the natural logarithm of the P-wave velocity, S-wave velocity, and density, respectively; $\mathbf{D}_1$ represents the first order difference matrix which can be written as:

$$\mathbf{D}_1 = \begin{bmatrix} -1 & 1 & 0 & \cdots & 0 \\ 0 & -1 & 1 & \cdots & 0 \\ \vdots & \ddots & \ddots & \ddots & \vdots \\ 0 & \cdots & 0 & -1 & 1 \end{bmatrix}. \tag{A.3}$$

The forward model for the first order term of Eq. (10) can be expressed as:

$$\mathbf{d}_1(\alpha) = \frac{1}{2}\mathbf{C}_1(\alpha)\mathbf{W}(\alpha)\mathbf{D}_1\mathbf{L}_\mathrm{P} + \frac{1}{2}\mathbf{C}_2(\alpha)\mathbf{W}(\alpha)\mathbf{D}_1\mathbf{L}_\mathrm{S} + \frac{1}{2}\mathbf{C}_3(\alpha)\mathbf{W}(\alpha)\mathbf{D}_1\mathbf{L}_\rho \tag{A.4}$$

with

$$\mathbf{C}_1(\alpha) = \frac{1}{2}\sec^2 \alpha,$$

$$\mathbf{C}_2(\alpha) = -4h^2 \sin^2 \alpha,$$

$$\mathbf{C}_3(\alpha) = \frac{1}{4} - h^2 \sin^2 \alpha$$

where $\mathbf{W}(\alpha)$ is the angle-dependent wavelet kernel matrix, $\mathbf{d}_1$ denotes the seismic data of the first order term. $\mathbf{C}_1(\alpha)$, $\mathbf{C}_2(\alpha)$, and $\mathbf{C}_3(\alpha)$ are the reflection coefficient angle matrix of the first-order terms, respectively.

Eq. (A.4) can be simplified and expressed in the form of a vector matrix as:

$$\mathbf{d}_1 = \mathbf{G}_1\mathbf{m} \tag{A.5}$$

with

$$\mathbf{d}_1 = \begin{bmatrix} \mathbf{d}_1(\alpha_1) \\ \mathbf{d}_1(\alpha_2) \\ \vdots \\ \mathbf{d}_1(\alpha_k) \end{bmatrix}, \mathbf{m} = \begin{bmatrix} \mathbf{L}_P \\ \mathbf{L}_S \\ \mathbf{L}_\rho \end{bmatrix},$$

$$\mathbf{G}_1 = \frac{1}{2}\begin{bmatrix} \mathbf{C}_1(\alpha_1)\mathbf{W}_1 & \mathbf{C}_2(\alpha_1)\mathbf{W}_1 & \mathbf{C}_3(\alpha_1)\mathbf{W}_1 \\ \mathbf{C}_1(\alpha_2)\mathbf{W}_2 & \mathbf{C}_2(\alpha_2)\mathbf{W}_2 & \mathbf{C}_3(\alpha_2)\mathbf{W}_2 \\ \vdots & \vdots & \vdots \\ \mathbf{C}_1(\alpha_k)\mathbf{W}_k & \mathbf{C}_2(\alpha_k)\mathbf{W}_k & \mathbf{C}_3(\alpha_k)\mathbf{W}_k \end{bmatrix}\mathbf{D}$$

where $\alpha_i (i = 1, 2, ..., k)$ is denoted as the angle of incidence. $\mathbf{W}_i$ represent seismic wavelet, which is a simplified expression for $\mathbf{W}(\alpha_i)$; $\mathbf{G}_1$ is the first-order forward operator; $\mathbf{m}$ is natural logarithm of the three elasticity parameters; $\mathbf{D} = kron(\mathbf{I}_{3\times3}, \mathbf{D}_1)$, where $kron$ is the Kronecker product and $\mathbf{I}_{3\times3}$ is the 3rd order identity matrix.

The forward model for the second order term of Eq. (10) can be expressed as:

$$\mathbf{d}_2 = \mathbf{G}_2[(\mathbf{Qm}) \circ (\mathbf{Qm})], \tag{A.6}$$

with

$$\mathbf{G}_2 = \begin{bmatrix} \mathbf{C}_4(\alpha_1)\mathbf{W}_1 & \mathbf{C}_5(\alpha_1)\mathbf{W}_1 & \mathbf{C}_6(\alpha_1)\mathbf{W}_1 \\ \mathbf{C}_4(\alpha_2)\mathbf{W}_2 & \mathbf{C}_5(\alpha_2)\mathbf{W}_2 & \mathbf{C}_6(\alpha_2)\mathbf{W}_2 \\ \vdots & \vdots & \vdots \\ \mathbf{C}_4(\alpha_k)\mathbf{W}_k & \mathbf{C}_5(\alpha_k)\mathbf{W}_k & \mathbf{C}_6(\alpha_k)\mathbf{W}_k \end{bmatrix}, \tag{A.7}$$

$$C_4(\alpha) = \frac{h^3 \sin\alpha \tan\alpha}{2\sqrt{1 - h^2\sin^2\alpha}}\left(1 - 2h^2\sin^2\alpha + \cos^2\alpha\right),$$

$$C_5(\alpha) = -\frac{2h^3\sin^3\alpha \tan\alpha}{\sqrt{1 - h^2\sin^2\alpha}},$$

$$C_6(\alpha) = -\frac{h\sin\alpha \tan\alpha}{\sqrt{1 - h^2\sin^2\alpha}}\left(\frac{1}{4} - \frac{1}{2}h^2\sin^2\alpha\right),$$

$$\mathbf{Q} = \begin{bmatrix} 0 & 2\mathbf{i} & \mathbf{i} \\ 0 & \mathbf{i} & 0 \\ 0 & 0 & \mathbf{i} \end{bmatrix}\mathbf{D},$$

where $\mathbf{G}_2$ represents the forward operator of the second order term. It is worth noting that in order to represent the quadratic terms, we introduce the Hadamard product operator denoted by $\circ$, then $[(\mathbf{Qm}) \circ (\mathbf{Qm})]$ can be rewritten as:

$$(\mathbf{Qm}) \circ (\mathbf{Qm}) = \begin{bmatrix} 2\Delta\mathbf{I}_S + \Delta\mathbf{I}_\rho \\ \Delta\mathbf{I}_S \\ \Delta\mathbf{I}_\rho \end{bmatrix} \circ \begin{bmatrix} 2\Delta\mathbf{I}_S + \Delta\mathbf{I}_\rho \\ \Delta\mathbf{I}_S \\ \Delta\mathbf{I}_\rho \end{bmatrix}$$

$$= \begin{bmatrix} (2\Delta\mathbf{I}_S + \Delta\mathbf{I}_\rho) \circ (2\Delta\mathbf{I}_S + \Delta\mathbf{I}_\rho) \\ \Delta\mathbf{I}_S \circ \Delta\mathbf{I}_S \\ \Delta\mathbf{I}_\rho \circ \Delta\mathbf{I}_\rho \end{bmatrix}, \tag{A.8}$$

The forward equation based on the quadratic PP reflectivity approximation can be expressed as:

$$\mathbf{d} = \mathbf{d}_1 + \mathbf{d}_2 = \mathbf{G}_1\mathbf{m} + \mathbf{G}_2((\mathbf{Qm}) \circ (\mathbf{Qm})) \tag{A.9}$$

References

Abreu, E.S.D., Castagna, J.P., Gil, G., 2019. Case study: phase-component amplitude variation with angle. Geophysics 84 (4), B285–B297. https://doi.org/10.1190/geo2018-0762.1.

Ajaz, M., Ouyang, F., Wang, G.H., et al., 2021. Fluid identification and effective fracture prediction based on frequency-dependent AVOAz inversion for fractured reservoirs. Pet. Sci. 18 (4), 1069–1085. https://doi.org/10.1016/j.petsci.2021.07.011.

Aki, K., Richards, P.G., 1980. Quantitative Seismology: Theory and Methods. W. H. Freeman and Company, San Francisco.

Chen, H.Z., Innanen, K.A., 2023. Estimating two groups of fracture weaknesses using azimuthal differences in partially incidence-angle-stacked seismic amplitudes. Geophysics 88 (4), R407–R419. https://doi.org/10.1190/geo2022-0541.1.

Chen, H.Z., Chen, T.S., Innanen, K.A., 2020a. Estimating tilted fracture weaknesses from azimuthal differences in seismic amplitude data. Geophysics 85 (3), R135–R146. https://doi.org/10.1190/geo2019-0344.1.

Chen, H.Z., Li, J.X., Innanen, K.A., 2020b. Inversion of differences in frequency components of azimuthal seismic data for indicators of oil-bearing fractured reservoirs based on an attenuative cracked model. Geophysics 85 (3), R163–R175. https://doi.org/10.1190/geo2019-0152.1.

Chen, H.Z., Pan, X.P., Ji, Y.X., et al., 2017. Bayesian Markov chain Monte Carlo inversion for weak anisotropy parameters and fracture weaknesses using azimuthal elastic impedance. Geophys. J. Int. 210 (2), 801–818. https://doi.org/10.1093/gji/ggx196.

Cheng, G.S., Yin, X.Y., Zong, Z.Y., 2019. Nonlinear elastic impedance inversion in the complex frequency domain based on an exact reflection coefficient. J. Pet. Sci. Eng. 178, 97–105. https://doi.org/10.1016/j.petrol.2019.03.023.

Conti, C.R., Roisenberg, M., Neto, G., Porsani, M.J., 2013. Fast seismic inversion methods using ant colony optimization algorithm. IEEE Geosci. Remote Sens. Lett. 10 (5), 1119–1123. https://doi.org/10.1109/LGRS.2012.2231397.

Dai, R.H., Yin, C, Peng, D., 2022. AVA inversion of pre-stack seismic data with cross-gradient constraints. J. Geophys. Appl. 199, 104594. https://doi.org/10.1016/j.jappgeo.2022.104594.

de Figueiredo, L.P., Grana, D., Bordignon, F.L., et al., 2018. Joint Bayesian inversion based on rock-physics prior modeling for the estimation of spatially correlated reservoir properties. Geophysics 83 (5), M49–M61. https://doi.org/10.1190/geo2017-0463.1.

de Figueiredo, L.P., Grana, D., Roisenberg, M., et al., 2019. Gaussian mixture Markov chain Monte Carlo method for linear seismic inversion. Geophysics 84 (3), R463–R476. https://doi.org/10.1190/geo2018-0529.1.

Ely, G., Malcolm, A., Poliannikov, O.V., 2018. Assessing uncertainties in velocity models and images with a fast nonlinear uncertainty quantification method. Geophysics 83 (2), R63–R75. https://doi.org/10.1190/geo2017-0321.1.

Fjeldstad, T., Grana, D., 2018. Joint probabilistic petro-physics seismic inversion based on Gaussian mixture and Markov chain prior models. Geophysics 83 (1), R31–R42. https://doi.org/10.1190/geo2017-0239.1.

Fjeldstad, T., Omre, H., 2020. Bayesian inversion of convolved hidden Markov models with applications in reservoir prediction. IEEE Trans. Geosci. Rem. Sens. 58 (3), 1957–1968. https://doi.org/10.1109/TGRS.2019.2951205.

Geman, S., Geman, D., 1984. Stochastic relaxation, Gibbs distributions, and the Bayesian restoration of images. IEEE Trans. Pattern Anal. Mach. Intell. 6 (6), 721–741. https://doi.org/10.1109/tpami.1984.4767596.

Grana, D., 2022. Bayesian rock-physics inversion with Kumaraswamy prior models. Geophysics 87 (3), M87–M97. https://doi.org/10.1190/geo2021-0469.1.

Guo, Q., Ba, J., Fu, L.Y., et al., 2021. Joint seismic and petrophysical nonlinear inversion with Gaussian mixture based adaptive regularization. Geophysics 86 (6), R895–R911. https://doi.org/10.1190/geo2021-0017.1.

Huang, G.T., Chen, X.H., Luo, C., et al., 2021. Geological structure-guided initial model building for prestack AVO/AVA inversion. IEEE Trans. Geosci. Rem. Sens. 59 (2), 1784–1793. https://doi.org/10.1109/TGRS.2020.2998044.

Li, C.H., Zhang, F.C., 2017. Amplitude-versus-angle inversion based on the L₁-norm-based likelihood function and the total variation regularization constraint. Geophysics 82 (3), R173–R182. https://doi.org/10.1190/geo2016-0182.1.

Li, K., Li, K., Yin, X.Y., et al., 2022a. Hierarchical Bayesian probabilistic seismic AVO inversion using Gibbs sampling with IA2RMS algorithm. IEEE Geosci. Remote Sens. Lett. 19, 1–5. https://doi.org/10.1109/LGRS.2022.3181816.

Li, K., Yin, X.Y., Zong, Z.Y., Grana, D., 2022b. Estimation of porosity, fluid bulk modulus, and stiff-pore volume fraction using a multitrace Bayesian amplitude-variation-with-offset petrophysics inversion in multiporosity reservoirs. Geophysics 87 (1), M25–M41. https://doi.org/10.1190/geo2021-0029.1.

Li, K., Yin, X.Y., Zong, Z.Y., et al., 2020. Direct estimation of discrete fluid facies and fluid indicators via a Bayesian seismic probabilistic inversion and a novel exact PP-wave reflection coefficient. J. Pet. Sci. Eng. 196 (3), 107412. https://doi.org/10.1016/j.petrol.2020.107412.

Li, L., Zhang, G.Z., Liu, J.Z., et al., 2021. Estimation of fracture density and orientation from azimuthal elastic impedance difference through singular value decomposition. Pet. Sci. 18 (6), 1675–1688. https://doi.org/10.1016/j.petsci.2021.09.037.

Martino, L., Read, J., Luengo, D., 2015. Independent doubly adaptive rejection metropolis sampling within Gibbs sampling. IEEE Trans. Signal Process. 63 (12), 3123–3138. https://doi.org/10.1109/TSP.2015.2420537.

Metropolis, N., Rosenbluth, A.W., Rosenbluth, M.N., et al., 1953. Equation of state calculations by fast computing machines. J. Chem. Phys. 21 (6), 1087–1092. https://doi.org/10.1063/1.1699114.

Pan, X.P., Li, L., Zhou, S.X., et al., 2021. Azimuthal amplitude variation with offset parameterization and inversion for fracture weaknesses in tilted transversely isotropic media. Geophysics 86 (1), C1–C18. https://doi.org/10.1190/geo2019-0215.1.

Pan, X.P., Zhang, G.Z., Zhang, J.J., et al., 2017. Zoeppritz-based AVO inversion using an improved Markov chain Monte Carlo method. Pet. Sci. 14 (1), 75–83. https://doi.org/10.1007/s12182-016-0131-4.

Pei, S., Yin, X.Y., Li, K., 2022. Improved fixed-point seismic inversion constrained by instantaneous phase. J. Pet. Sci. Eng. 215, 110653. https://doi.org/10.1016/j.petrol.2022.110653.

Robert, C.P., Elvira, V., Tawn, N., Wu, C., 2018. Accelerating MCMC algorithms. WIREs Comput. Stat. 10 (5), e1435. https://doi.org/10.1002/wics.1435.

Rüger, A., 1997. P-wave reflection coefficients for transversely isotropic models with vertical and horizontal axis of symmetry. Geophysics 62 (3), 713–722. https://doi.org/10.1190/1.1444181.

Rüger, A., 2002. Reflection Coefficients and Azimuthal AVO Analysis in Anisotropic Media. SEG.

Wang, Y., 1999. Approximations to the Zoeppritz equations and their use in AVO analysis. Geophysics 64 (6), 1920–1927. https://doi.org/10.1190/1.1444698.

Yang, Y.M., Xia, X.T., Yin, X.Y., et al., 2022. Data-driven fast prestack structurally constrained inversion. Geophysics 87 (3), N31–N43. https://doi.org/10.1190/geo2021-0145.1.

Yang, Y.M., Yin, X.Y., Li, K., et al., 2023. A linearized alternating direction method of multipliers algorithm for prestack seismic inversion in VTI media using the quadratic PP-Reflectivity approximation. IEEE Trans. Geosci. Rem. Sens. 61, 1–18. https://doi.org/10.1109/TGRS.2023.3267734.

Yin, X.Y., Zong, Z.Y., Wu, G.C., 2015. Research on seismic fluid identification driven by rock physics. Sci. China Earth Sci. 58 (2), 159–171. https://doi.org/10.1007/s11430-014-4992-3.

Yu, S.H., Zong, Z.Y., Yin, X.Y., et al., 2023. Rock physics and seismic reflectivity parameterization and amplitude variation with offsets inversion in terms of total organic carbon indicator. Pet. Sci. 20 (4), 2092–2112. https://doi.org/10.1016/j.petsci.2023.02.012.

Zhang, F.C., Dai, R.H., Liu, H.Q., 2015. High order approximation for scattering matrix in layered elastic medium and its application in pre-stack seismic inversion. J. Pet. Sci. Eng. 131, 210–217. https://doi.org/10.1016/j.petrol.2015.04.026.

Zhang, J.Z., Taflanidis, A.A., 2019. Accelerating MCMC via Kriging-based adaptive independent proposals and delayed rejection. Comput. Methods Appl. Mech. Eng. 355, 1124–1147. https://doi.org/10.1016/j.cma.2019.07.016.

Zhi, L.X., Chen, S.Q., Li, X.Y., 2016. Amplitude variation with angle inversion using the exact Zoeppritz equations—theory and methodology. Geophysics 81 (2), N1–N15. https://doi.org/10.1190/geo2014-0582.1.

Zhou, L., Li, J.Y., Yuan, C., et al., 2022. Bayesian deterministic inversion based on the exact reflection coefficients equations of transversely isotropic media with a vertical symmetry axis. IEEE Trans. Geosci. Rem. Sens. 60, 1–15. https://doi.org/10.1109/TGRS.2022.3176628.

Zoeppritz, K., 1919. On the reflection and propagation of seismic waves. Gottinger Nachrichten 1 (5), 66–84.

Zuo, Y.H., Zong, Z.Y., Li, K., Luo, K., 2024. Bayesian AVOAz inversion of fluid and anisotropy parameters using Gibbs sampling with AISM algorithm. IEEE Trans. Geosci. Rem. Sens. 62, 1–15. https://doi.org/10.1109/TGRS.2024.3484435.